

## Supporting Information

# **Yolk-Shell Hierarchical Catalyst with Tremella-Like Molybdenum Sulfide on Transition Metal (Co, Ni and Fe) Sulfide for Electrochemical Water Splitting**

*Tao Yang,<sup>a\*</sup> Lisi Yin,<sup>a</sup> Maoshuai He,<sup>b,e</sup> Wenxian Wei,<sup>c</sup> Guojian Cao,<sup>d</sup> Xinran Ding,<sup>a</sup> Yihui Wang,<sup>a</sup> Ziming Zhao,<sup>a</sup> Tingting Yu,<sup>a</sup> Hong Zhao<sup>a</sup> and Dongen Zhang<sup>a</sup>*

<sup>a</sup> School of Chemical Engineering, Jiangsu Ocean University, Lianyungang 222005 (China)

<sup>b</sup> State Key Laboratory of Eco-Chemical Engineering, Ministry of Education, College of Chemistry and Molecular Engineering, Qingdao University of Science and Technology, Qingdao 266042 (China)

<sup>c</sup> Testing Center, Yangzhou University, Yangzhou 225009 (China)

<sup>d</sup> School of Materials Science and Engineering, Harbin University of Science and Technology, Harbin 150040 (China)

<sup>e</sup> School of Materials Science and Engineering, Shandong University of Science and Technology, Qingdao 266590 (China)

Corresponding author: yangtao\_hit@163.com

## **Experimental Section**

### **Materials**

All chemicals are of analytical grade and were used as received without further purification. Cobalt (II) acetate (99.99 %), nickel (II) nitrate hexahydrate (99.99 %), potassium ferricyanide (99.95 %), trisodium citrate dehydrate (99 %), sublimed sulfur (99.95 %), ammonium tetrathiomolybdate (99.95 %) and DMF (99.8 %) were purchased from Aladdin Industrial Corporation.

### **Synthesis of CoNi-Fe PBA particles**

Cobalt (II) acetate (53 mg), nickel (II) nitrate hexahydrate (87.5 mg) and trisodium citrate dihydrate (264.3 mg) were dissolved in water (20 mL). Potassium ferricyanide (131.1 mg) was dissolved in water (20 mL). The above two solutions were mixed uniformly after ultrasonic treatment (30 min) and then reacted in a Teflon-lined stainless-steel autoclave at 28 °C for 20 h. The precipitate was then washed with water and ethanol for three times.

### **Synthesis of yolk-shell structured PBA-S particles**

CoNi-Fe PBA (28 mg) and sublimed sulfur (8.8 mg) were dispersed in DMF (12 mL), then sealed in a Teflon-lined stainless-steel autoclave and reacted at 190 °C for 20 h. The product was washed with ethanol for three times.

### **Synthesis of YS-MoS and H-MoS particles**

YS-MoS was prepared as following: PBA-S (28 mg) and ammonium tetrathiomolybdate (16.2 mg) were dispersed in a mixture of water (5 mL) and DMF (10 mL), then sealed in a Teflon-lined stainless-steel autoclave and reacted at 190 °C for 20 h. H-MoS was prepared through the same procedure except that the PBA-S was replaced by CoNi-Fe PBA (26.5 mg) and the reacting temperature was 210 °C. For comparison, pristine MoS<sub>2</sub> were prepared by putting ammonium tetrathiomolybdate (20 mg) into the mixture of water (5 mL) and DMF (10 mL) and reacted at 210 °C for 20 h. The above three products were washed with ethanol for three times.

### **Characterization**

Morphologies of the products were tested by using a JEM-2100 TEM and a FEI apreo SEM. EDS spectroscopy was performed on the TEM equipped with EDXA. Element distribution on the PBA-S nanoparticles was achieved by using a Tecnai-G2-F30 S-TWIN, which was equipped with a HAADF detector. HRTEM and HAADF-STEM of H-MoS and YS-MoS were tested on a Talos F200x G2. The element in the near surface layers was demonstrated with XPS, which was carried out on an ESCALAB 250Xi system. The PXRD spectrum of the

samples were obtained on a X'Pert PROM MPD (Panalytical) system with a CuK  $\alpha$  X-ray sources ( $\lambda = 1.5406$ ).

### **Preparation of samples for HER and OER electro-catalysis**

The catalyst slurry was prepared by mixing active material (5 mg) with pure carbon (Vulcan XC72, 2.5 mg) in a mixture of water (0.65 mL), ethanol (0.3 mL) and Nafion (5 % w/w in water and 1-propanol, 50  $\mu\text{m}$ ) with stirring.<sup>1</sup> A drop of the mixed solution (9  $\mu\text{L}$ ) was transferred onto a rotating disk electrode (RDE, 0.196  $\text{cm}^2$ ) with a pipette. After drying in airflow, the electrode was used for HER and OER test. As to the carbon paper electrodes, the slurry was repeatedly daubed onto a piece of carbon paper (1 $\times$ 1  $\text{cm}^2$ ). The net weight of the catalyst on the carbon paper was 2.8 mg. After drying in airflow, the carbon paper electrodes were used as both anode and cathode for the overall water splitting test.

### **Electrochemical characterizations**

HER and OER electro-catalysis tests were performed in a typical three-electrode configuration with a PGSTAT-302N instrument. RDE with active sample was used as the working electrode, Hg/HgO as the reference electrode and a Pt foil (1.0  $\text{cm}^2$ ) as the counter electrode. All of the polarization curves were measured in 1.0 M KOH solution using RDE with 1600 r.p.m. at a scan rate of 5  $\text{mVs}^{-1}$ . Chronoamperometric responses (i-t) were recorded on YS-MoS using RDE with 1600 r.p.m. for 1800 s at a constant over-potential of 285 mV (vs. RHE) for HER and 178 mV (vs. RHE) for OER. The electrochemical double-layer capacitance was used as an indicator for ECSA. One cycle of potential sweeping was carried out using RDE at 1600 r.p.m. at six different scan rates (10, 20, 40, 80, 120 and 1600  $\text{mVs}^{-1}$ ). Absolute value of the measured capacitive current densities at the average potential in the selected range were added and plotted as a function of the scan rates, the slope of the linear fit was used as an indicator for ECSA. Overall water splitting was tested in a two-electrode system using the carbon paper electrodes with active samples as both the cathode and anode. For the gas production measurements, the hydrogen and oxygen produced at 10  $\text{mA cm}^{-2}$  were quantitatively collected by the drainage method at 298 K for 180 min. The faradic efficiency was calculated with the following equation:<sup>2</sup>

$$FE = \frac{m \times n \times F}{I \times t} \times 100\%$$

Where, m is the moles of hydrogen or oxygen, mol; n is the electrons transfer for gas, 2 for hydrogen and 4 for oxygen; F is the Faraday constant; I is the current, A; t is time, s.

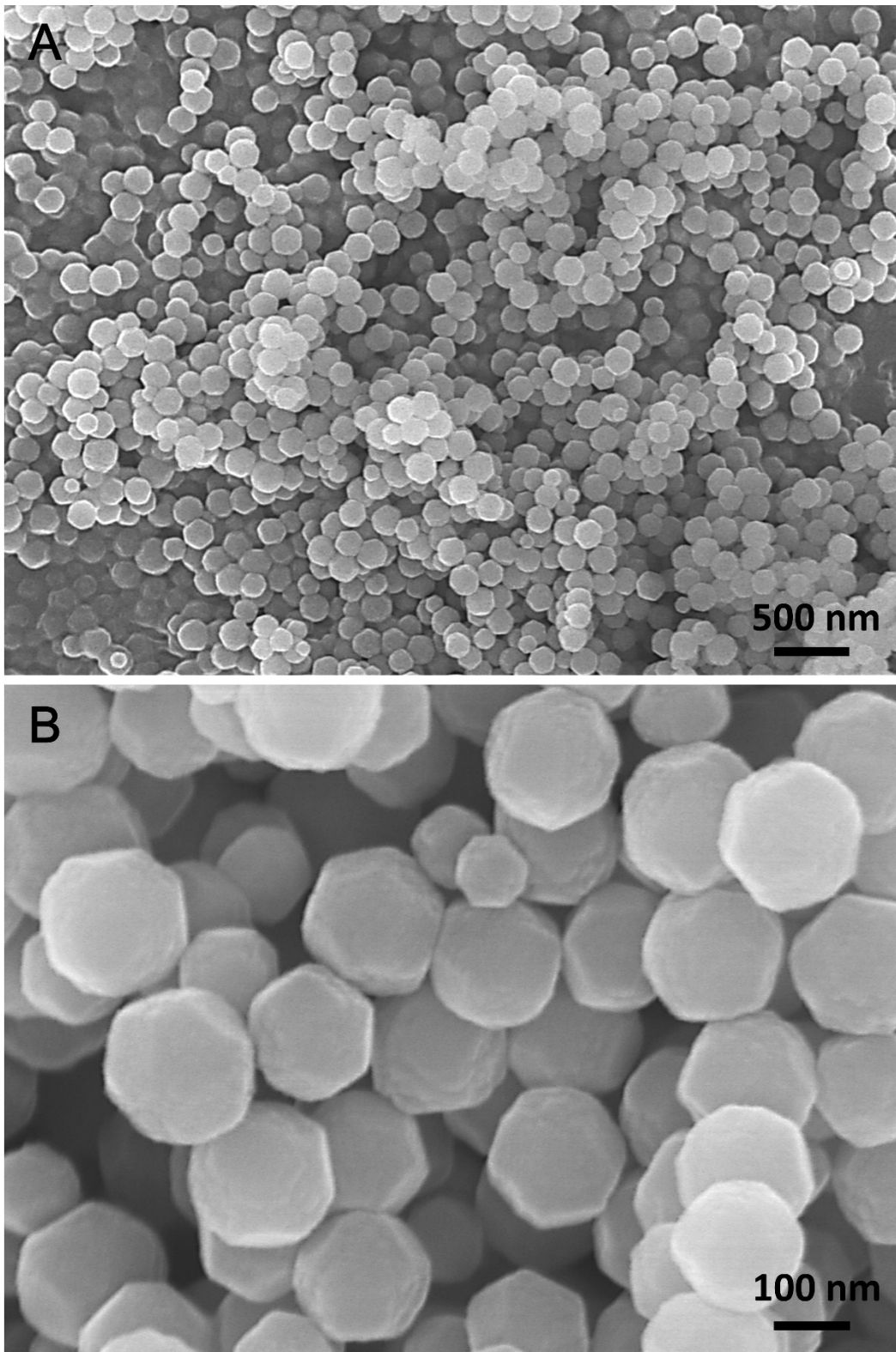


**Fig. S1.** SEM of CoNi-Fe PBA at different magnifications. The as-obtained CoNi-Fe PBAs are dominantly polyhedral shape with rough edges and corners

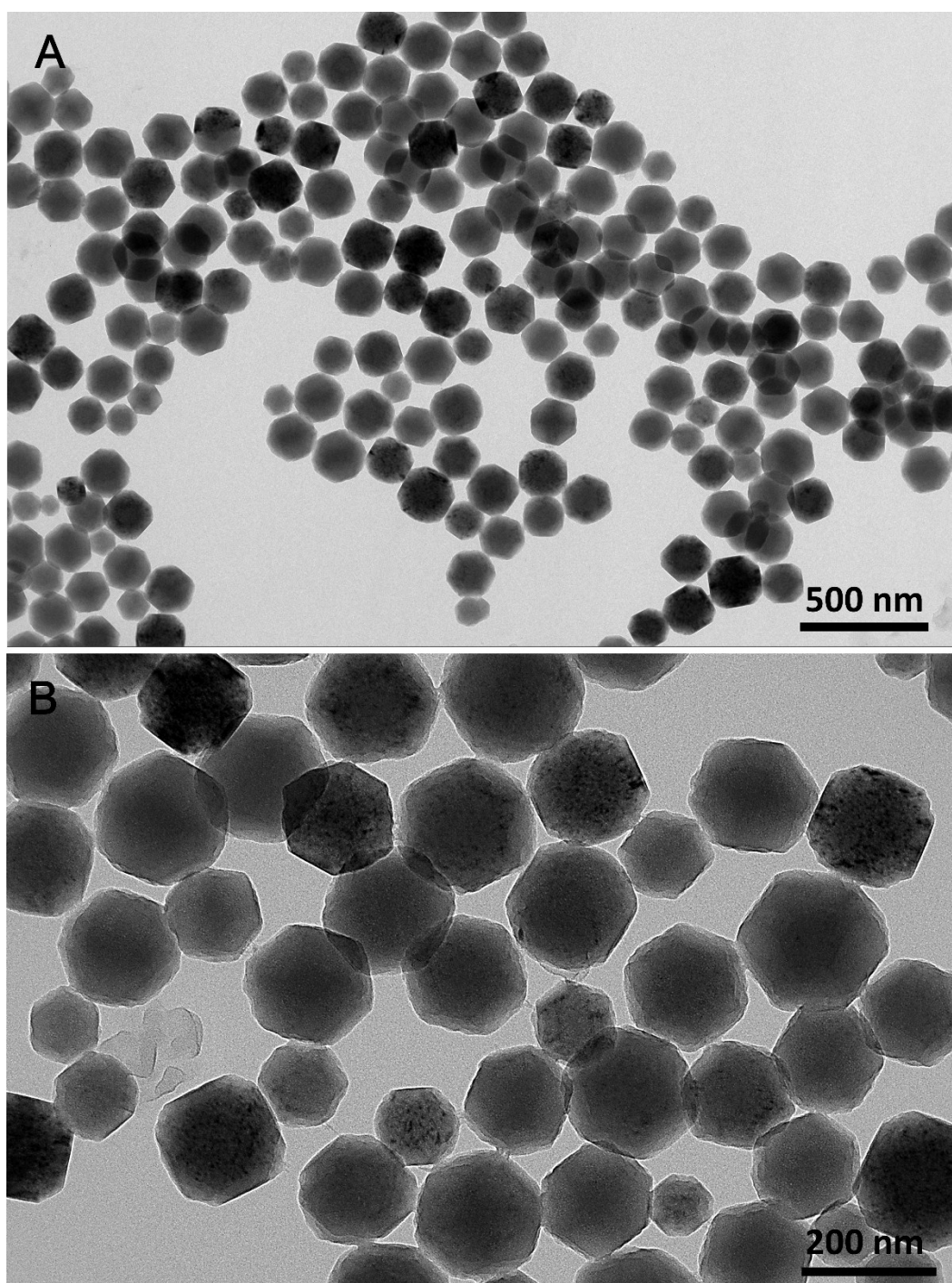


**Fig. S2.** TEM images of CoNi-Fe PBA at different magnifications. All the particles are polyhedral shape and below 150 nm.

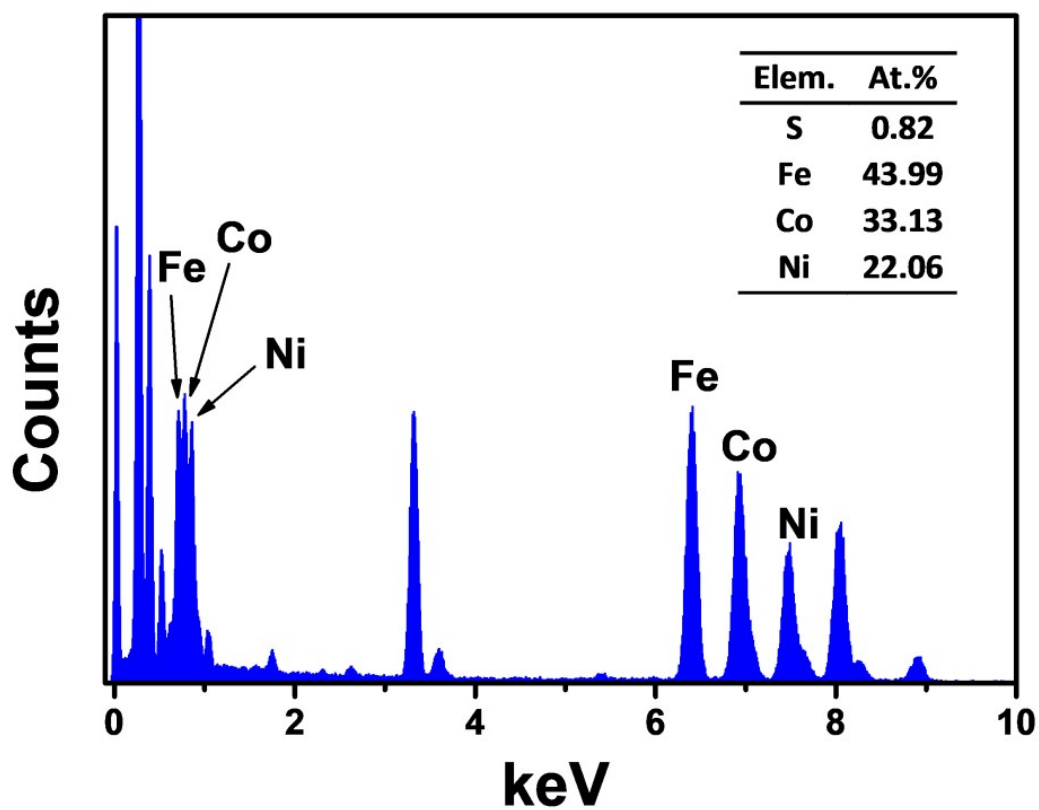


**Fig. S3.** EDS spectra of CoNi-Fe PBA and the corresponding composition. The atomic ratios of Co, Ni and Fe are 43.99 %, 33.13 % and 22.06 %, respectively.

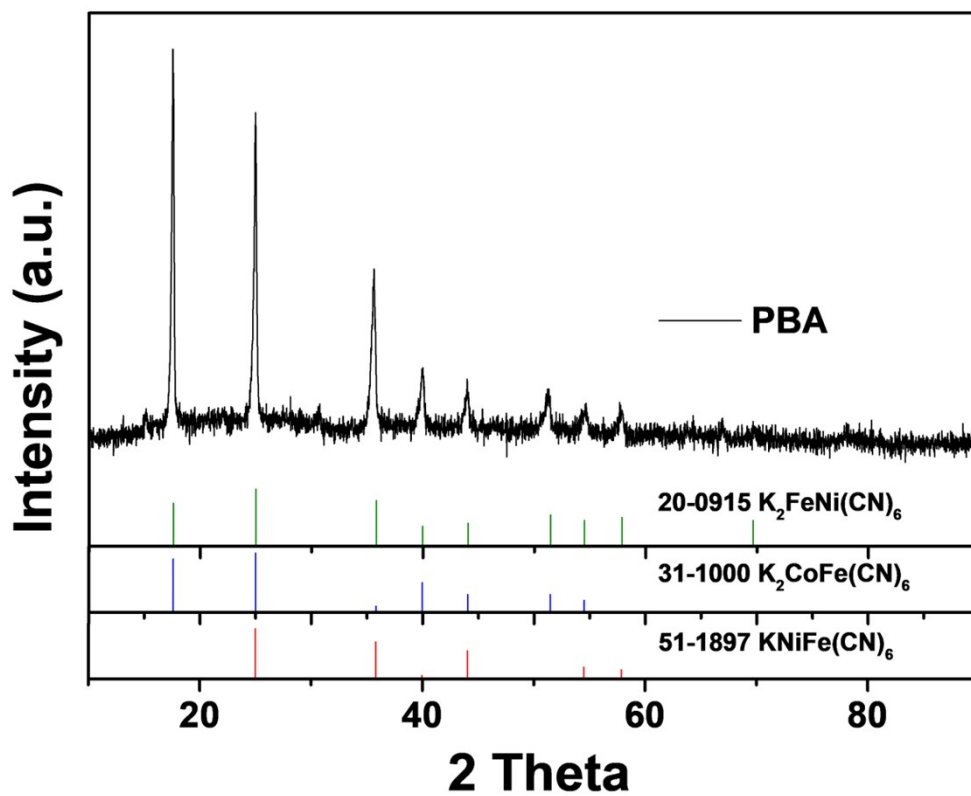


**Fig. S4.** XRD spectra of CoNi-Fe PBA. Nearly all the peaks can be assigned to the compounds of  $\text{K}_2\text{CoFe(CN)}_6$ ,  $\text{K}_2\text{FeNi(CN)}_6$  and  $\text{KNiFe(CN)}_6$ .

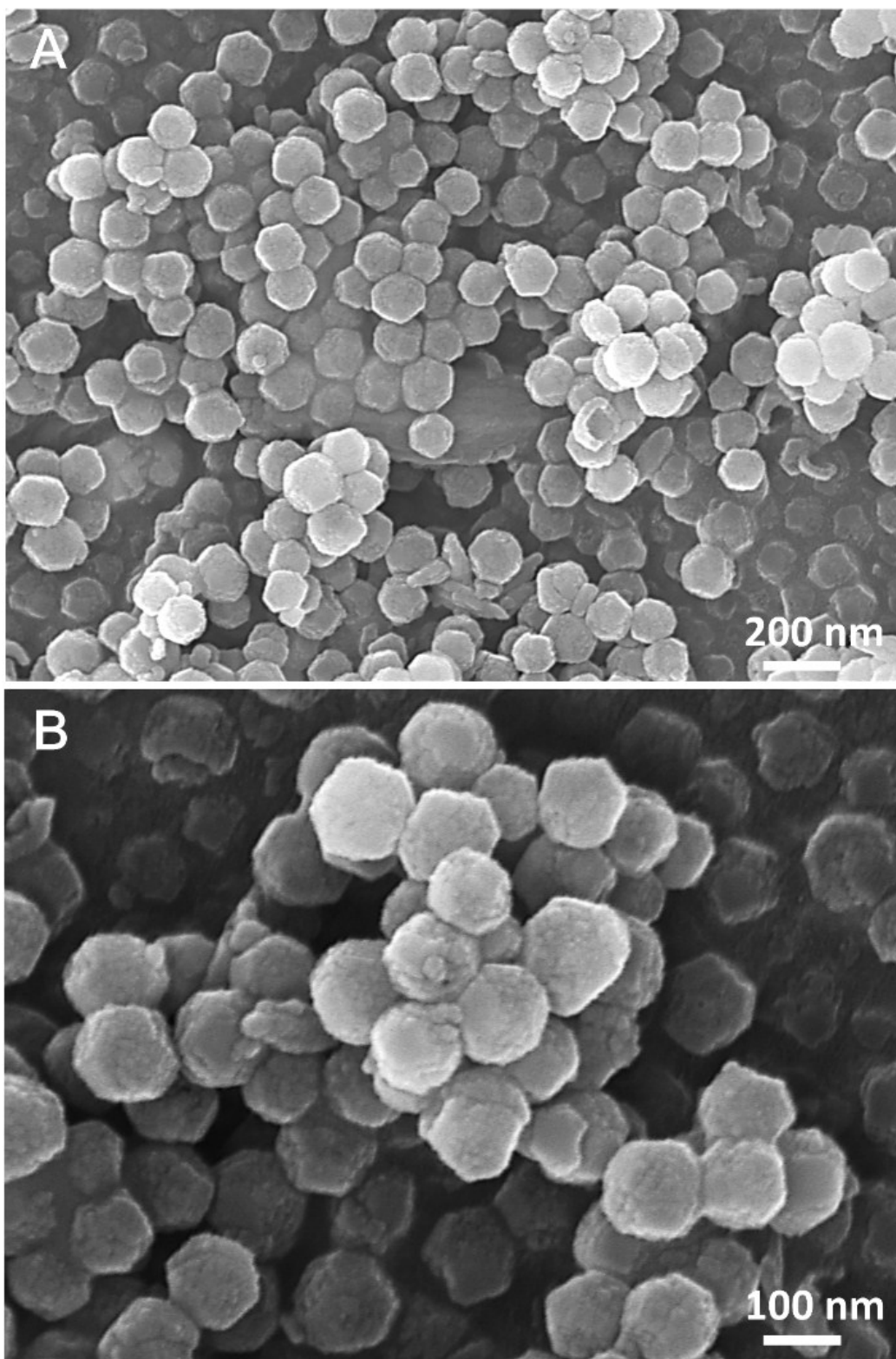


**Fig. S5.** SEM images of PBA-S, that was obtained by reacting CoNi-Fe PBA with sulfur powder in DMF at 190 °C. The yolk-shell structure can be observed from some cracked particles. The PBA-S particles preserved polyhedral shape and have similar size with PBA precursor, but much rougher surface.

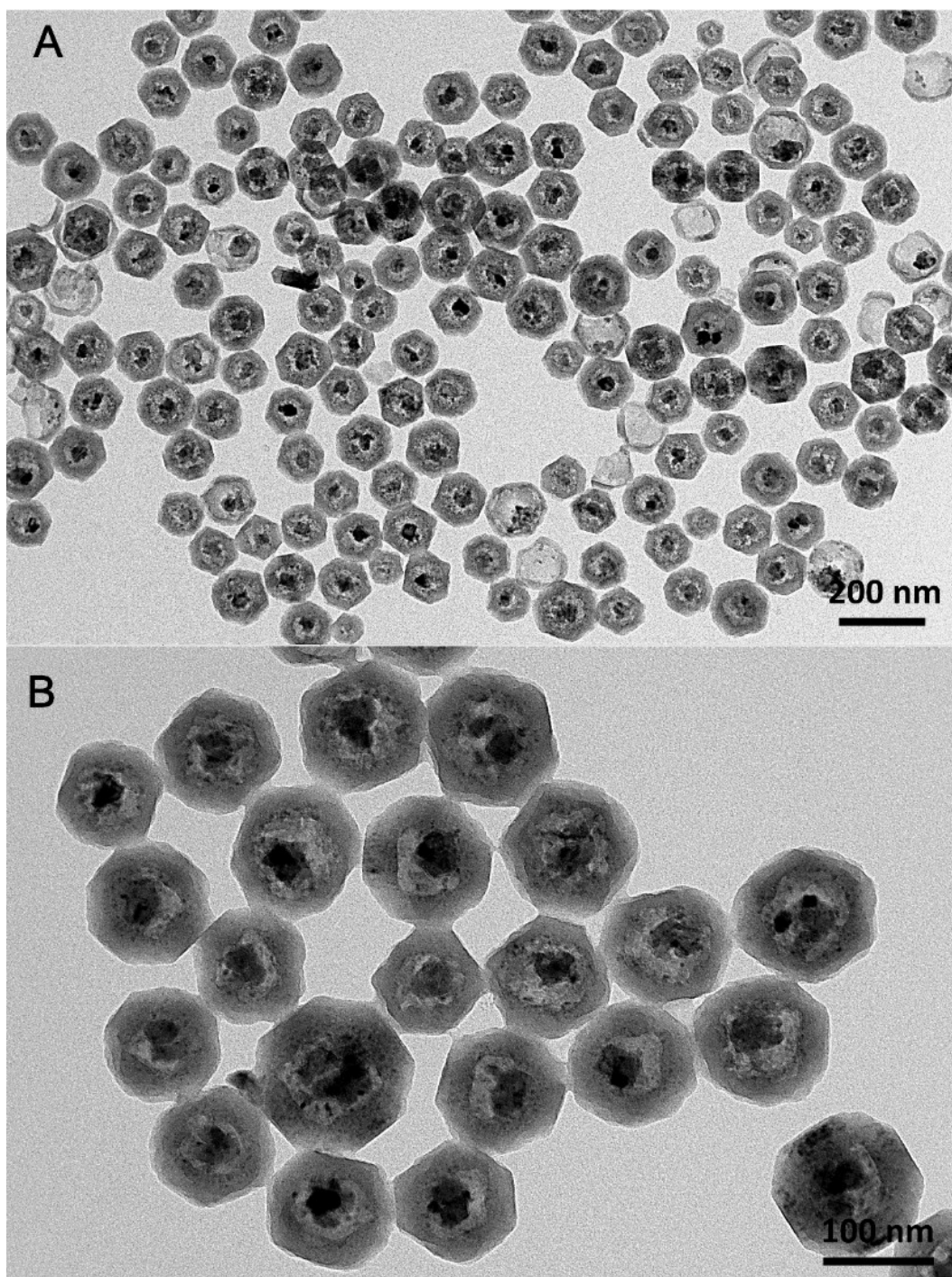


**Fig. S6.** TEM images of PBA-S, that was obtained by reacting CoNi-Fe PBA with sulfur powder in DMF at 190 °C. Nearly all the particles are yolk-shell structure. The yolks with an average diameter of 30-40 nm are enclosed by the separated shells with an average thickness of 20-30 nm.

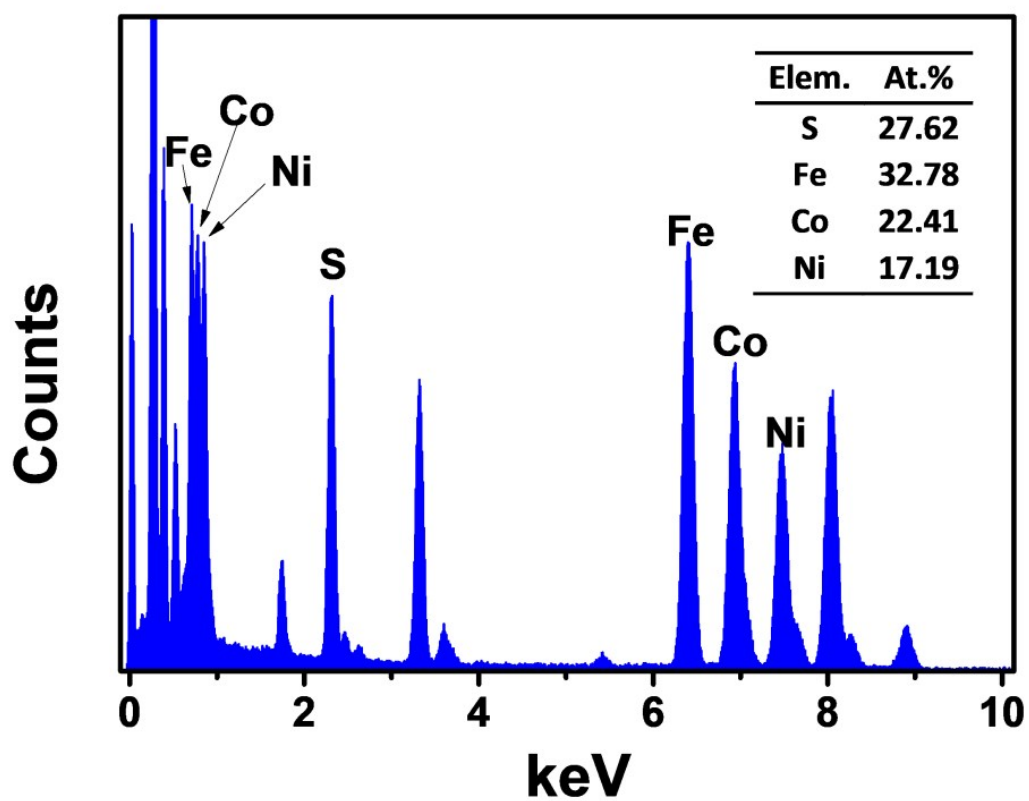


**Fig. S7.** EDS spectra and the corresponding composition of PBA-S, that was obtained by reacting CoNi-Fe PBA with sulfur powder in DMF at 190 °C. The atomic ratio of S increased up to 27.62 %.

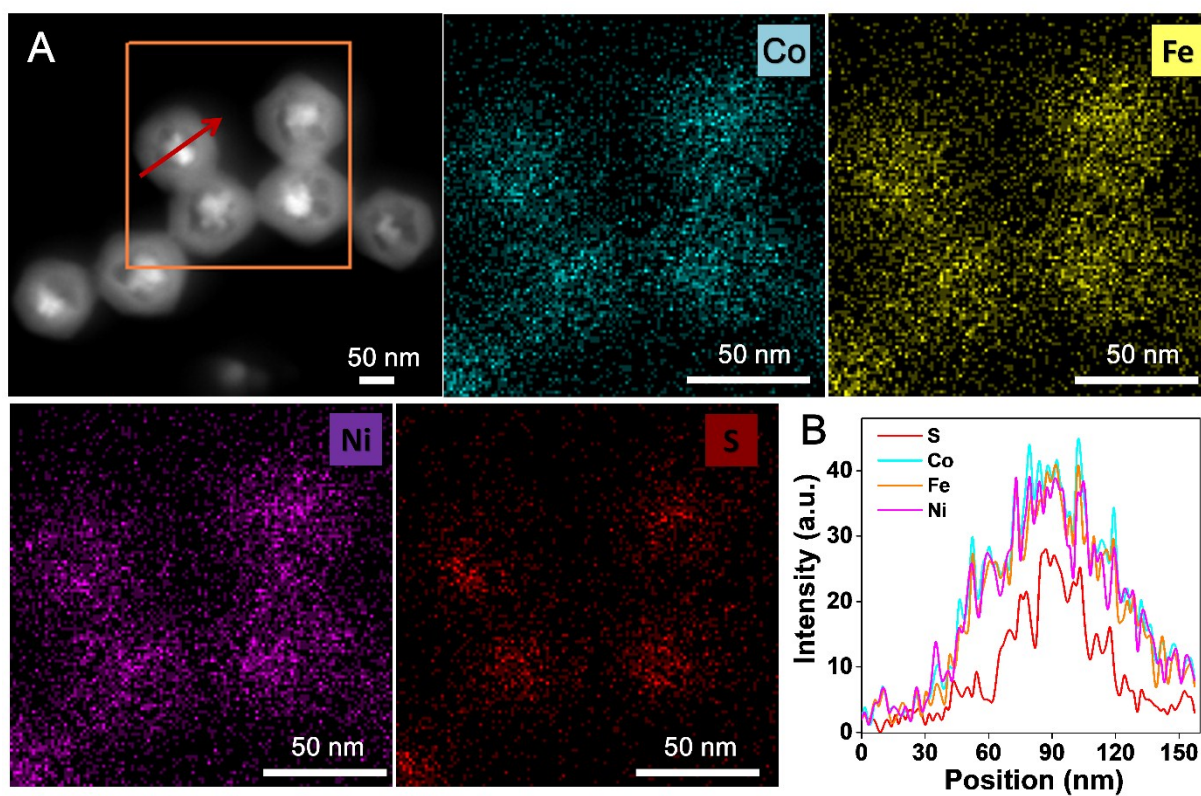


**Fig. S8.** (A) HAADF-STEM image and the corresponding elements mapping of PBA-S particles, Co (cyan), Fe (yellow), Ni (purple), S (red). (B) EDX cross-sectional compositional line scanning profile. The S content in the shell is slightly lower, which might be attributed to the existence of metal oxide formed during the sulfuration process.

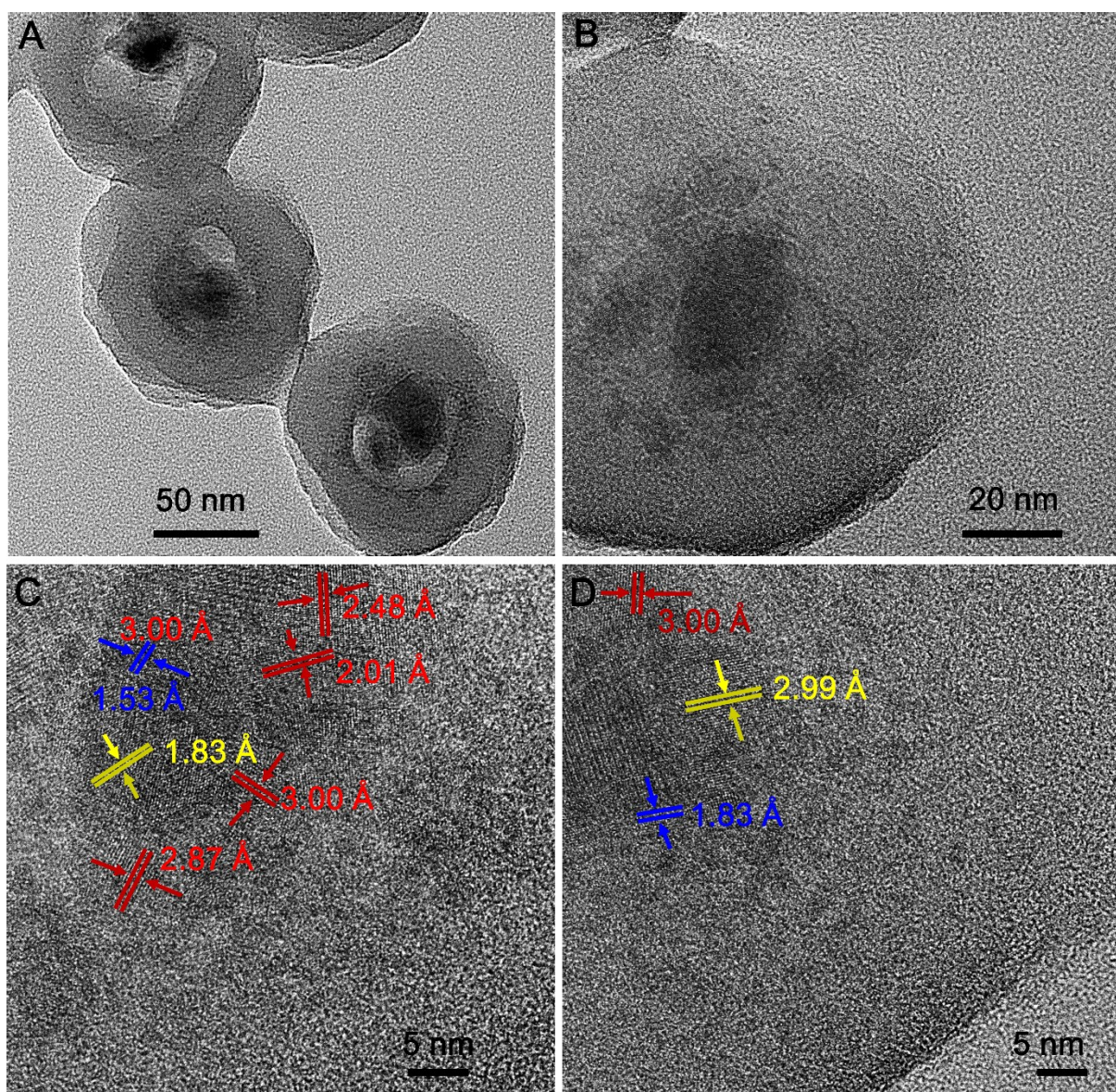


**Fig. S9.** HRTEM of PBA-S. (A) and (B) HRTEM of PBA-S particles, (C) and (D) enlarged region of (C). The red lattice fringes are assigned to  $\text{Co}_9\text{O}_8$ , the blue fringes are assigned to  $\text{N}_{2.824}\text{S}_2$ , the yellow fringes are assigned to  $\text{Fe}_{4.50}\text{Ni}_{4.50}\text{S}_{7.80}$ .

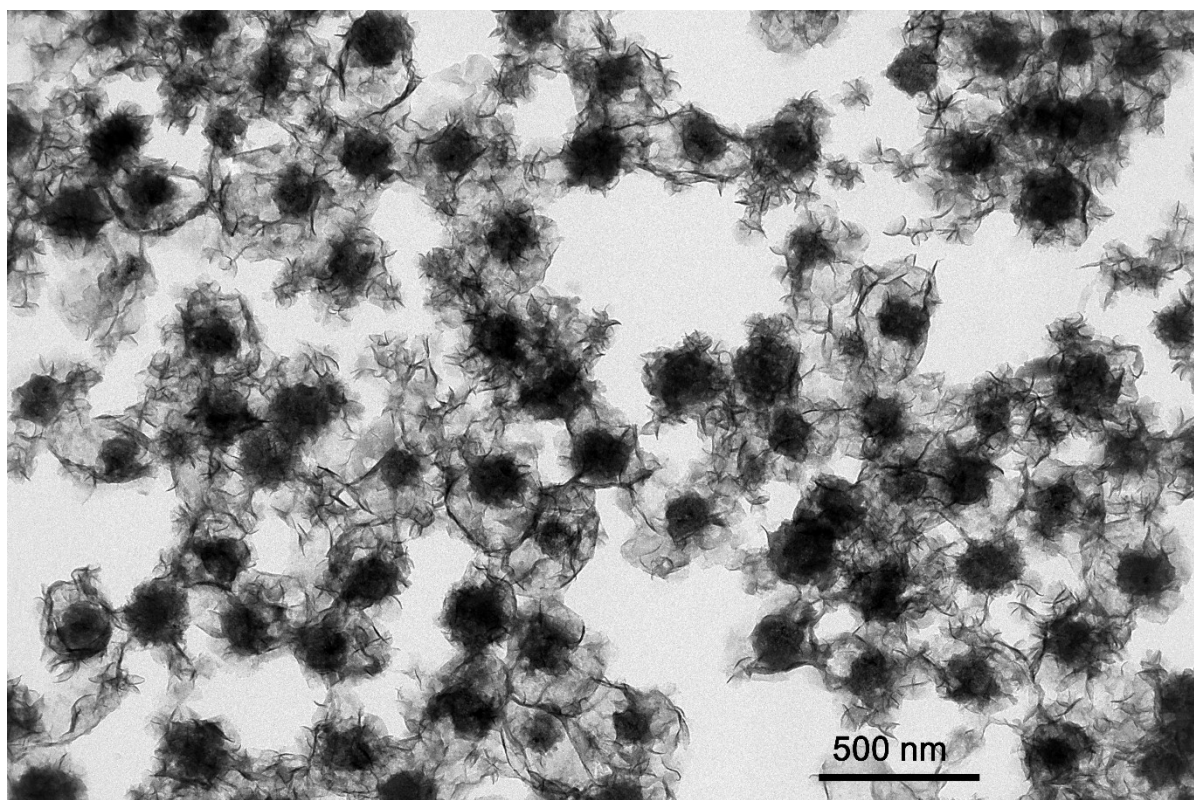


**Fig. S10.** TEM image of YS-MoS<sub>2</sub>, that was obtained by reacting PBA-S with (NH<sub>4</sub>)<sub>2</sub>MoS<sub>4</sub> in a mixture of DMF and water at 210 °C for 20 h. All the particles are yolk-shell structured and constructed by many randomly assembled MoS<sub>2</sub> nano-sheets on a solid core. The yolk-shell structured MoS<sub>2</sub> particles demonstrates a water-saturated tremella configuration.<sup>3</sup>

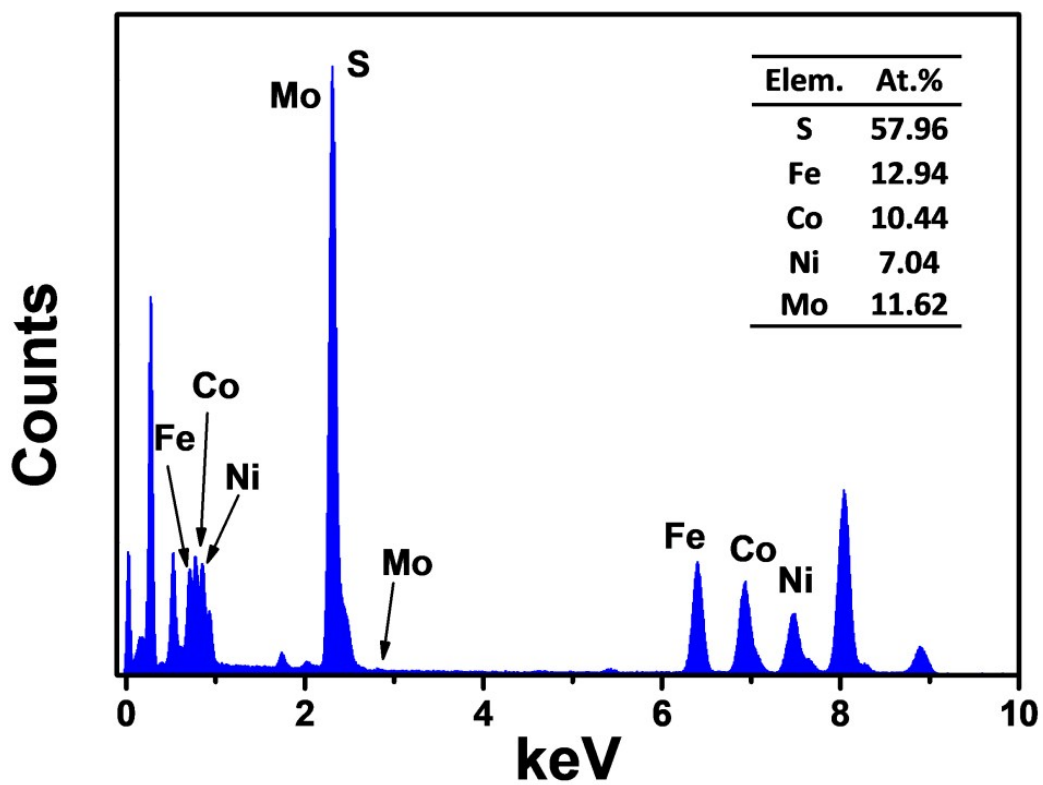


**Fig. S11.** EDS spectra and the corresponding composition of YS-MoS, that was obtained by reacting PBA-S with  $(\text{NH}_4)_2\text{MoS}_4$  in a mixture of DMF and water at 210 °C for 20 h. The atomic ratios of Fe, Co and Ni are slightly higher than H-MoS.

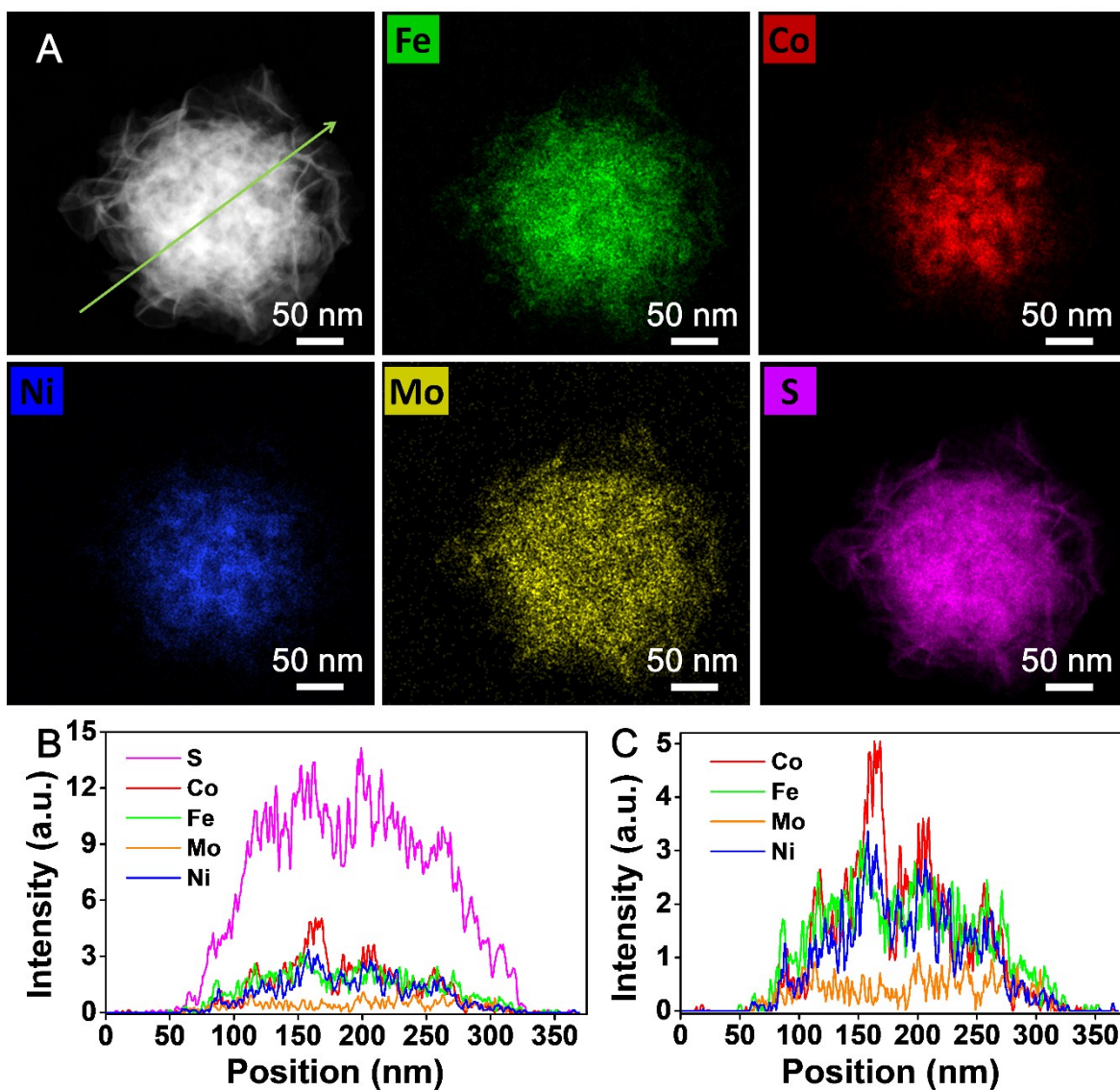


**Fig. S12.** HAADF-STEM image and corresponding element scanning of an individual YS-MoS particle. (A) HAADF-STEM image and corresponding EDX mapping of Fe(green), Co(red), Ni(blue), Mo(yellow) and S(pink). (B, C) EDX cross-sectional compositional line scanning profile and the magnified compositional line without S showing that Mo is mainly dispersed on the shell rather than the yolk.

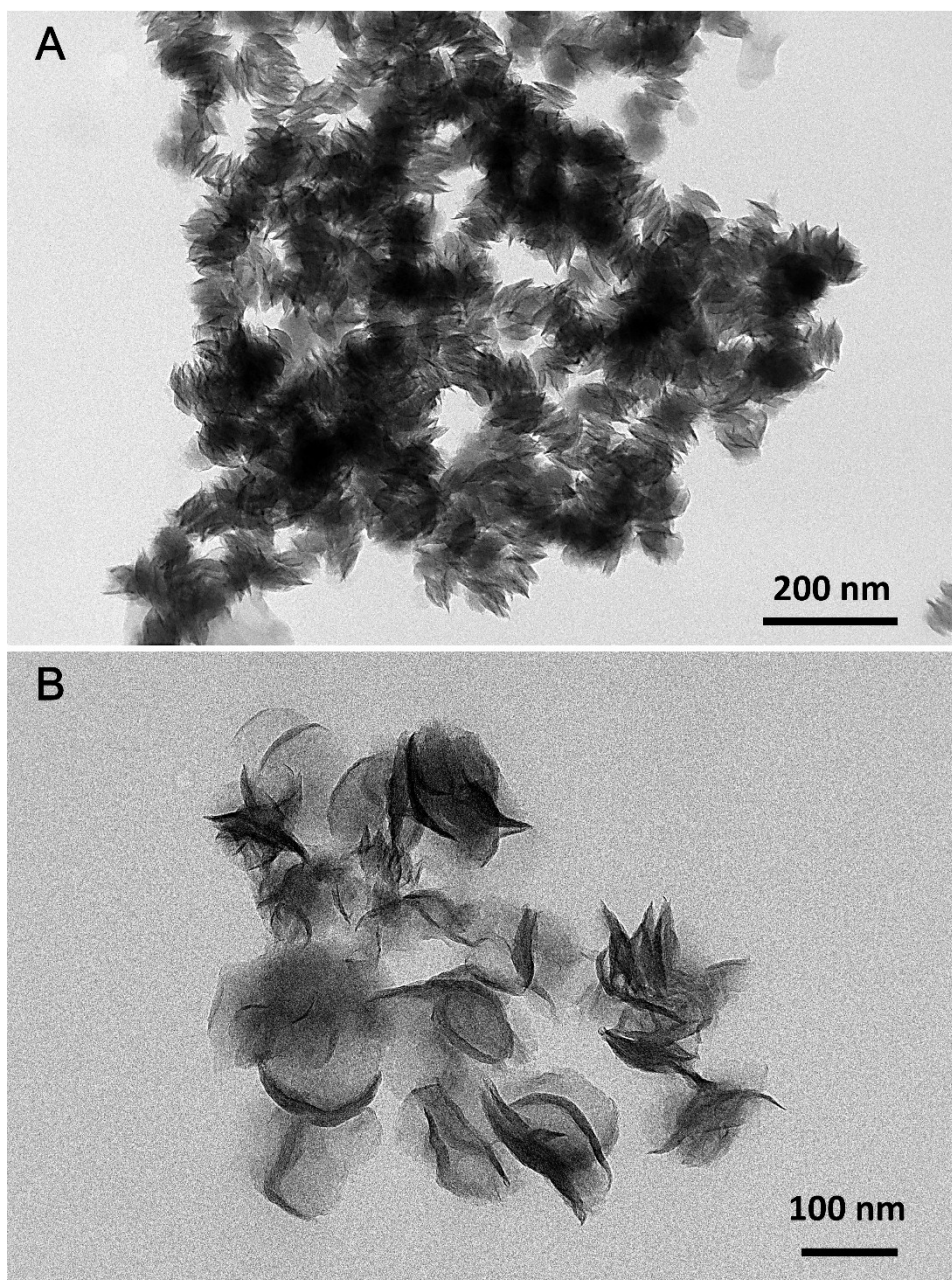


**Fig. S13.** TEM images of stacked MoS<sub>2</sub> nano-sheets at (A) low and (B) high magnifications. The stacked MoS<sub>2</sub> were produced by putting tetrathiomolybdate (20 mg) into the mixture of water (5 mL) and DMF (10 mL) and reacted at 190 °C for 20 h .

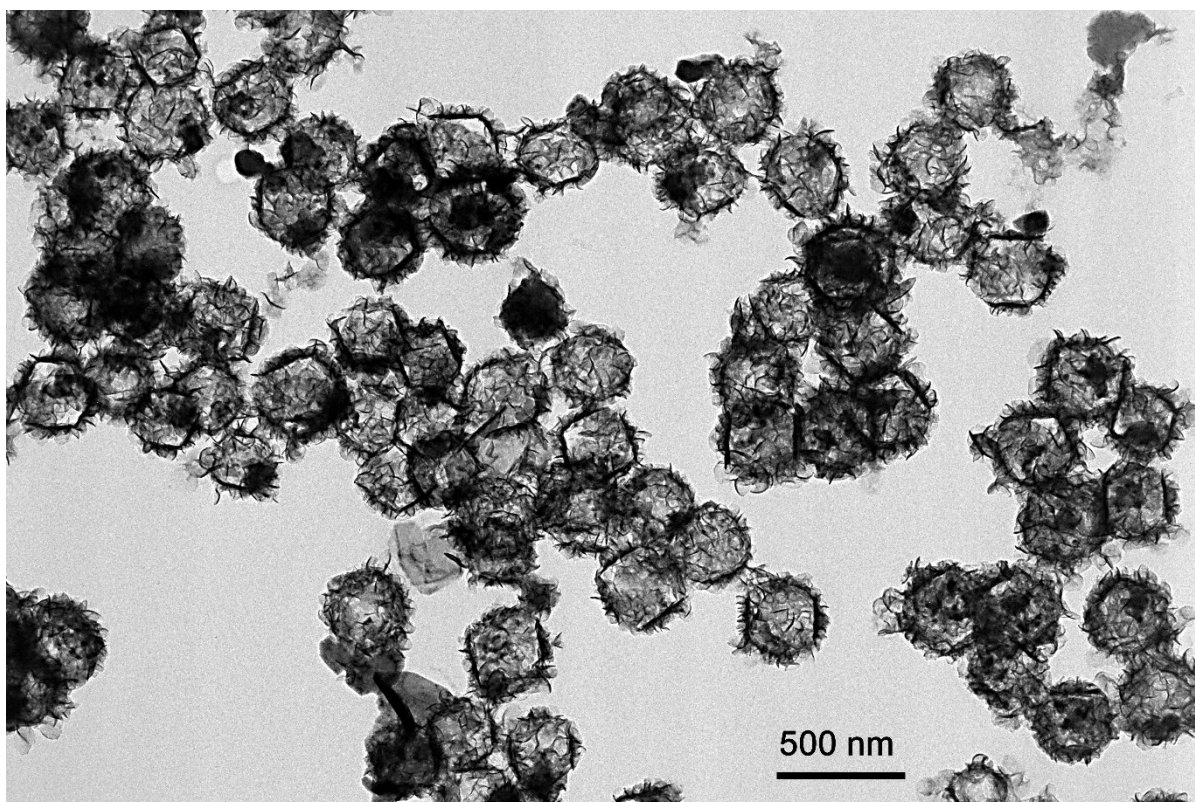


**Fig. S14.** TEM image of H-MoS<sub>2</sub>, that was obtained by reacting PBA with (NH<sub>4</sub>)<sub>2</sub>MoS<sub>4</sub> in a mixture of DMF and water at 210 °C for 20 h. All the particles are hollow structured and constructed by many randomly assembled MoS<sub>2</sub> nano-sheets.

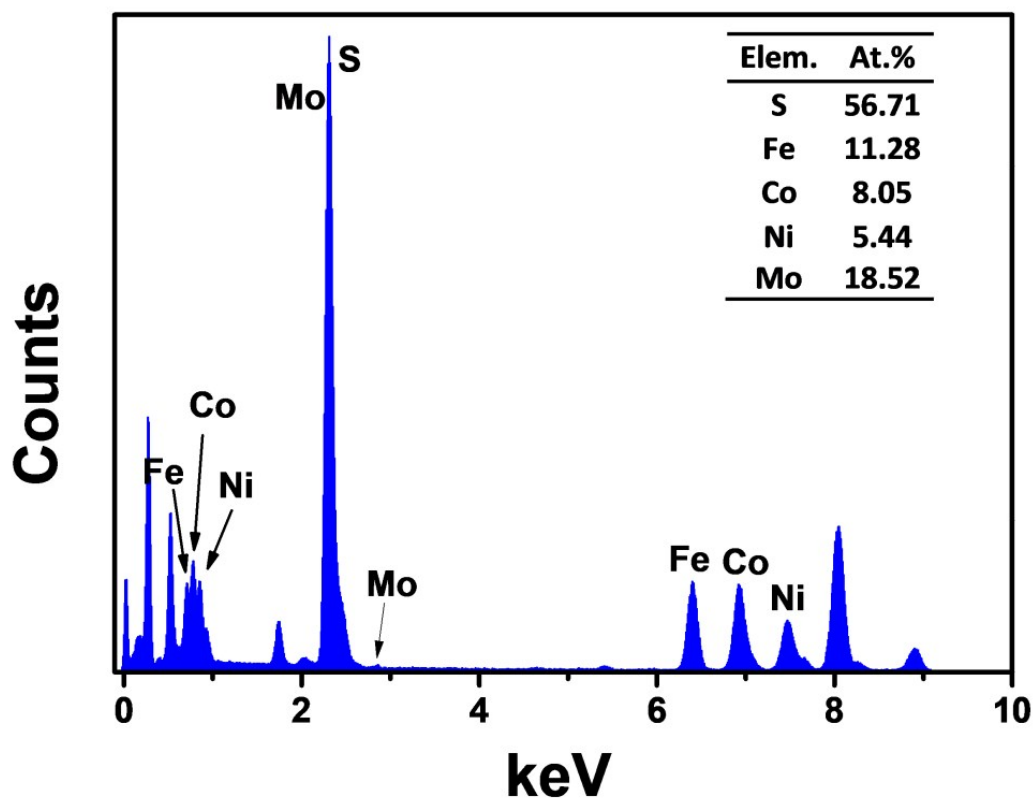


**Fig. S15.** EDS spectra and the corresponding composition of H-MoS<sub>4</sub>, that was obtained by reacting PBA with (NH<sub>4</sub>)<sub>2</sub>MoS<sub>4</sub> in a mixture of DMF and water at 210 °C for 20 h. The TM atoms of Fe, Co and Ni are still existence in the hollow particles and the atomic ratio of S increased greatly.

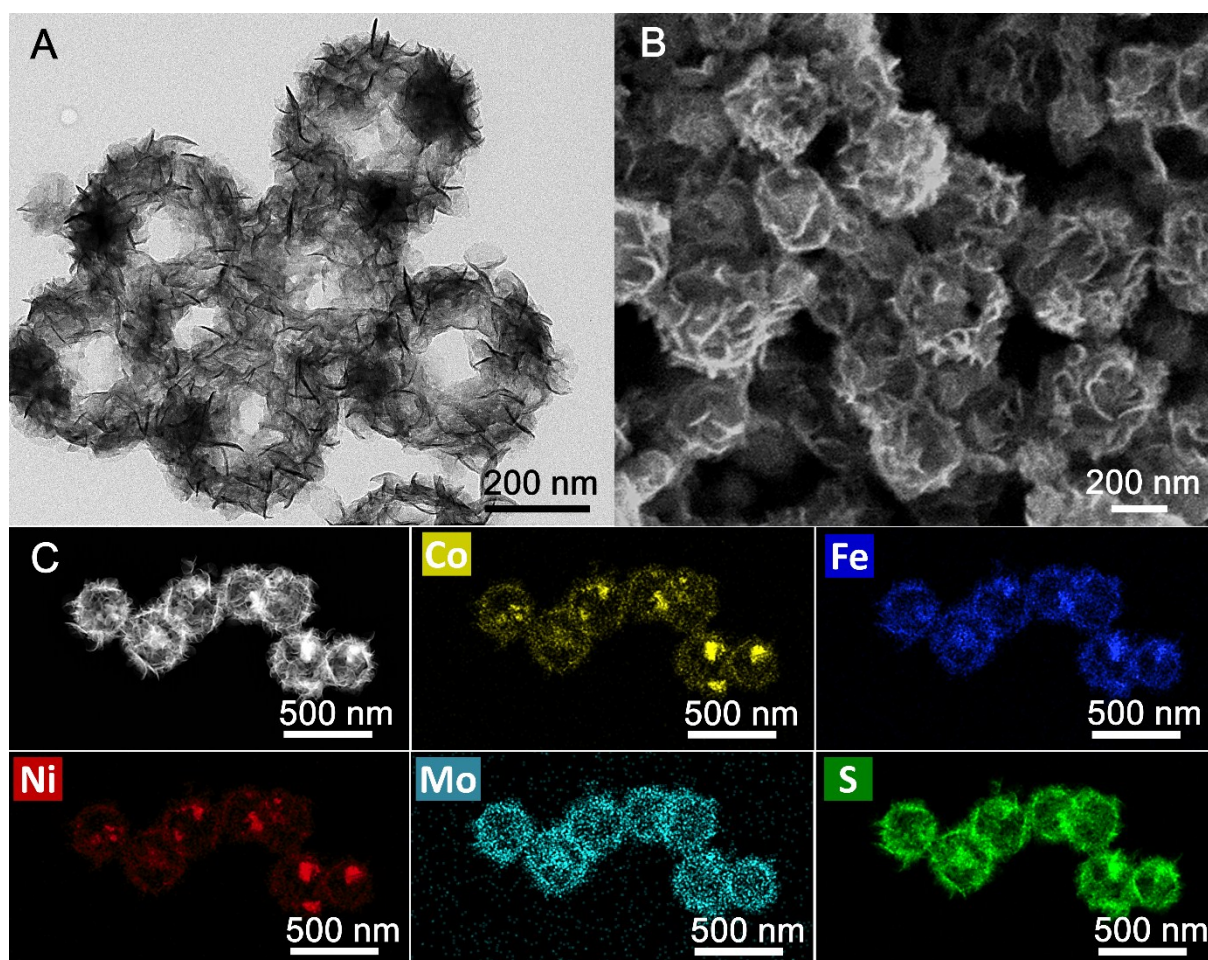


**Fig. S16.** Morphologies and structure of hollow structure. (A, B) TEM and SEM images showing the hollow structure and the tremella-like  $\text{MoS}_2$  nanosheets. (C) HAADF-STEM image and corresponding element scanning of several hollow particles.

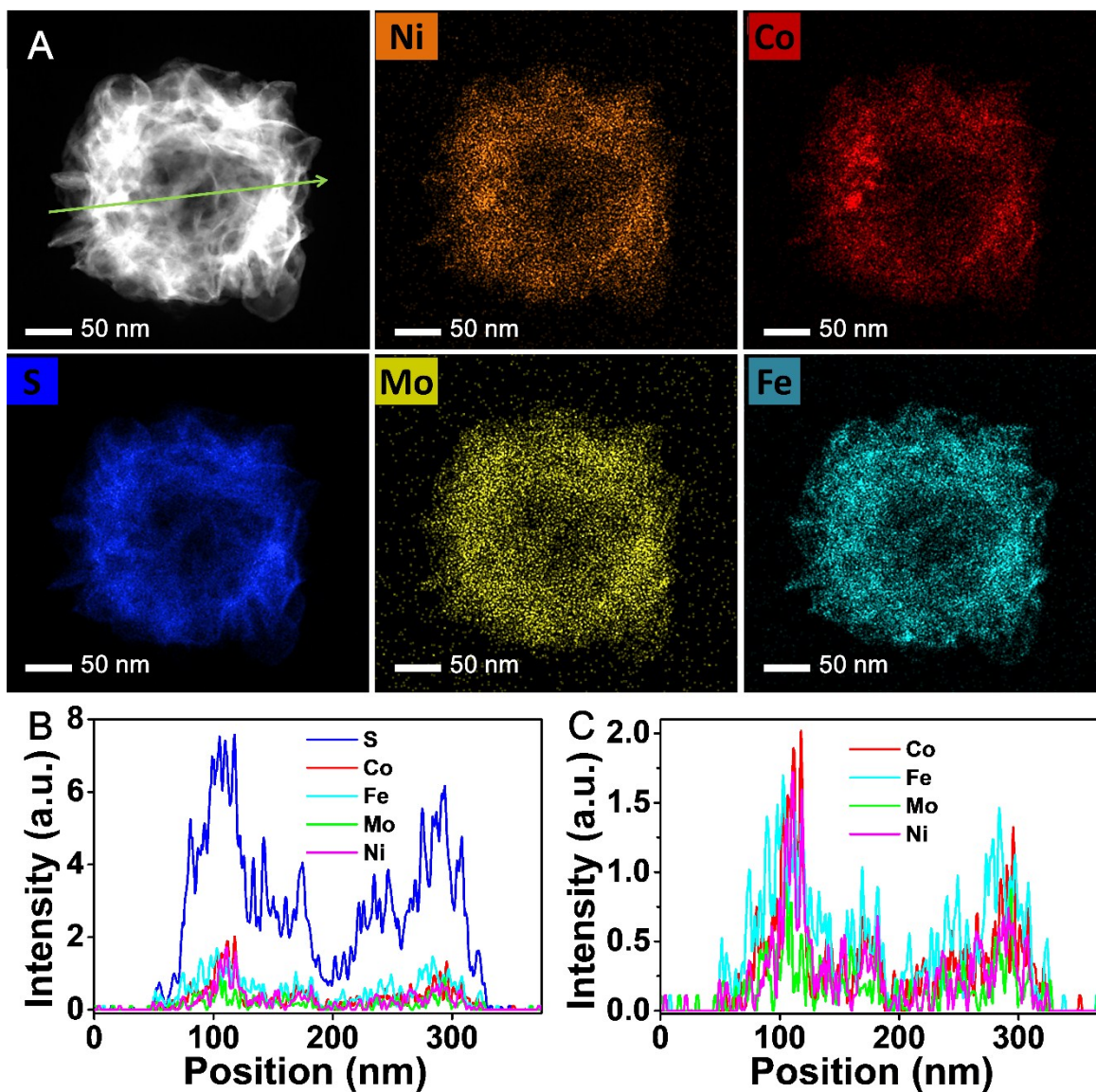


**Fig. S17.** HAADF-STEM image and corresponding element scanning of an individual H-MoS particle. (A) HAADF-STEM image and corresponding EDX mapping of Ni(orange), Co(red), S(blue), Mo(yellow) and Fe(cyan) showing the uniform elements distribution on the H-MoS particle. (B, C) EDX cross-sectional compositional line scanning profile and the magnified compositional line without S along with the detecting line.

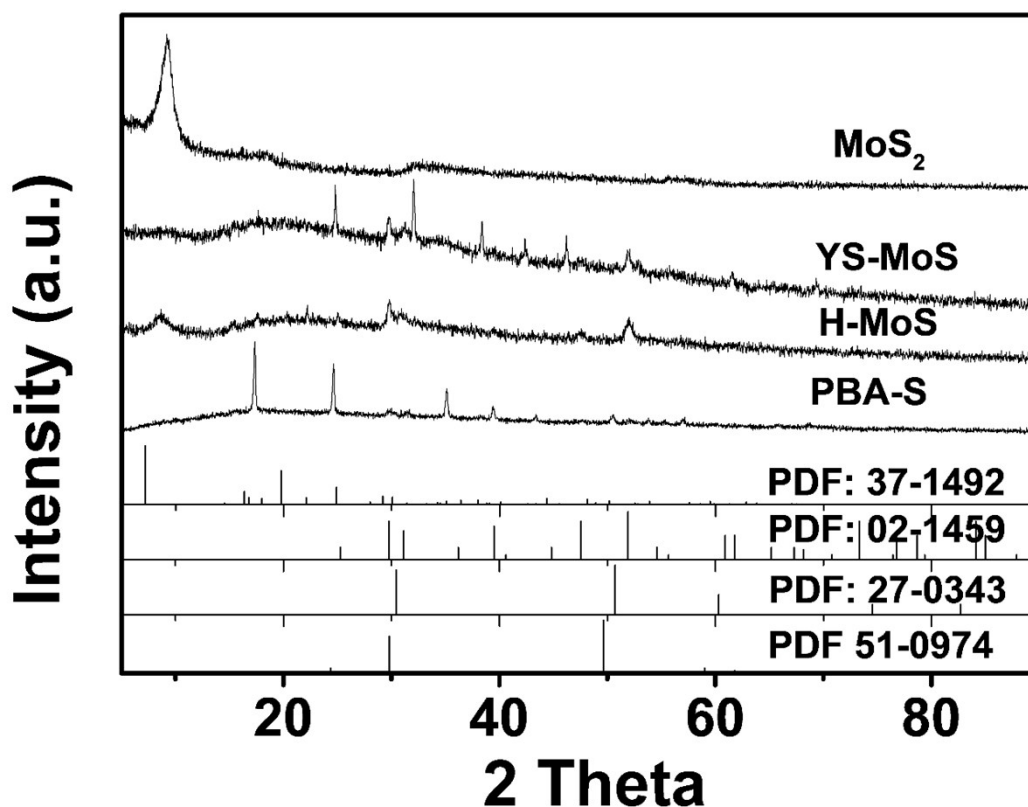


**Fig. S18.** XRD spectra of YS-MoS, H-MoS, bare MoS<sub>2</sub> and PBA-S. XRD pattern indicates the existence of TM sulfides (PDF: Co<sub>9</sub>S<sub>8</sub>: 02-1459, Ni<sub>3</sub>S<sub>2</sub>: 27-0343, Fe<sub>4.5</sub>Ni<sub>4.5</sub>S<sub>7.8</sub>: 51-0974) in PBA-S. Some diffraction peaks of TM sulfides appear in H-MoS, illustrating the formation of TM sulfides during the growth of MoS<sub>2</sub>. In the XRD pattern of pristine MoS<sub>2</sub>, the two peaks centered at 9.14° and 18.38° can be assigned to the (002) and (004) diffractions.<sup>4</sup> Compared with the pristine MoS<sub>2</sub>, the diffraction peaks of H-MoS shift toward smaller angles, suggesting the expanded interlayer spacing of the lamellar structure probably arising from the intercalation of Fe, Ni, Co or oxidized DMF into the MoS<sub>2</sub> layers.<sup>4a,4b</sup> Other diffraction peaks of MoS<sub>2</sub> are very weak, which may be due to the lack of long-range of atomic arrangement perpendicular to the nano-sheets with few layers.<sup>5</sup>

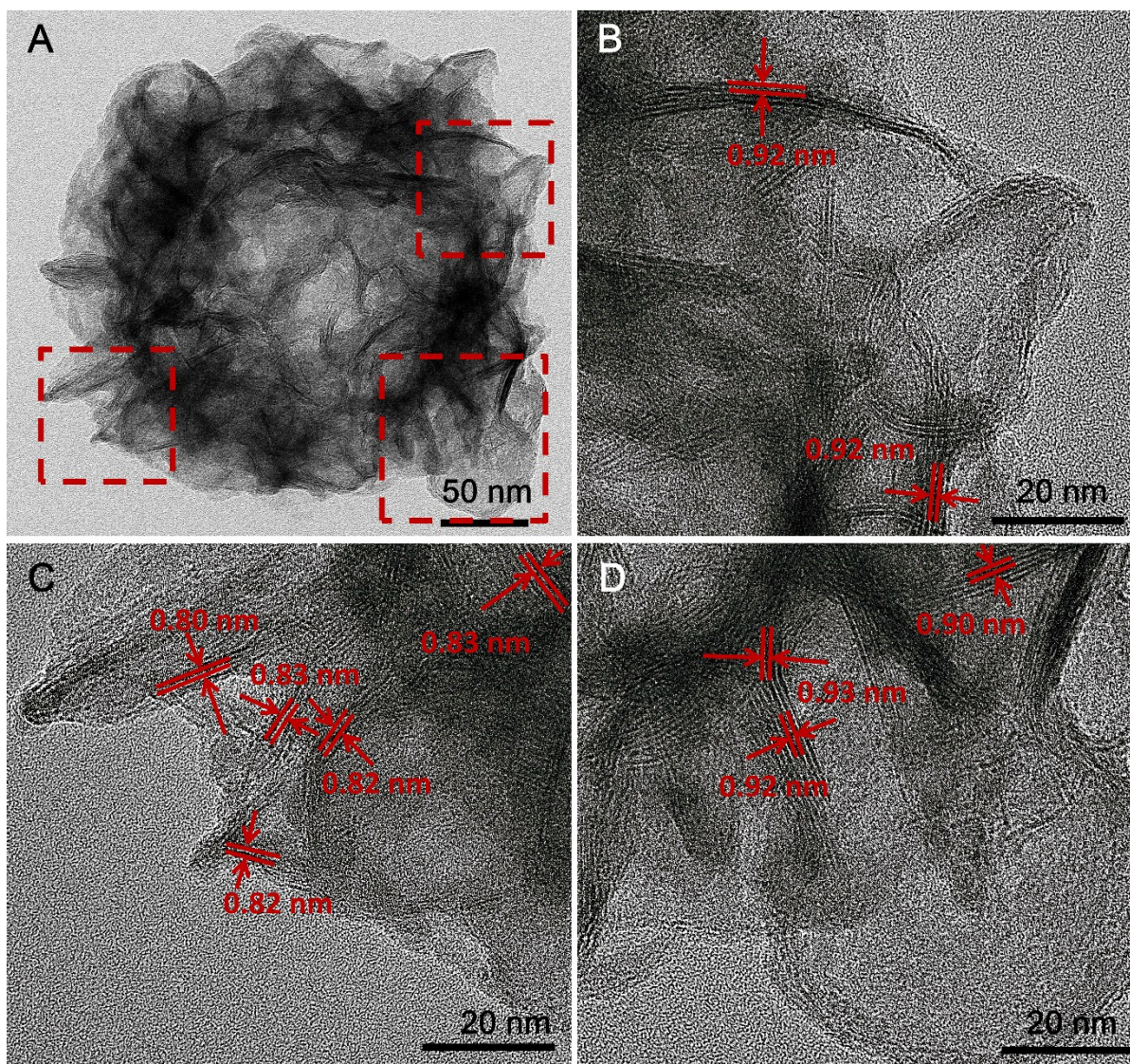


**Fig. S19.** HRTEM images of H-MoS. (A-D) HRTEM image of an individual H-MoS particle and three local regions showing the exposed edges, expanded interlayer and the layers number of the nano-sheets. The shell is constructed with many disordered and interlaced nano-sheets, while every sheet is assembled by several curved MoS<sub>2</sub> layers. The curvature and the not more than five layers revealed the ultrathin nature of the nano-sheets. The interlayer space of MoS shell is in the range of 0.80-0.95 nm, much larger than that of the pristine MoS<sub>2</sub>.<sup>6</sup> Such a larger interlayer space indicates the better separation of MoS<sub>2</sub> layers.<sup>7</sup>

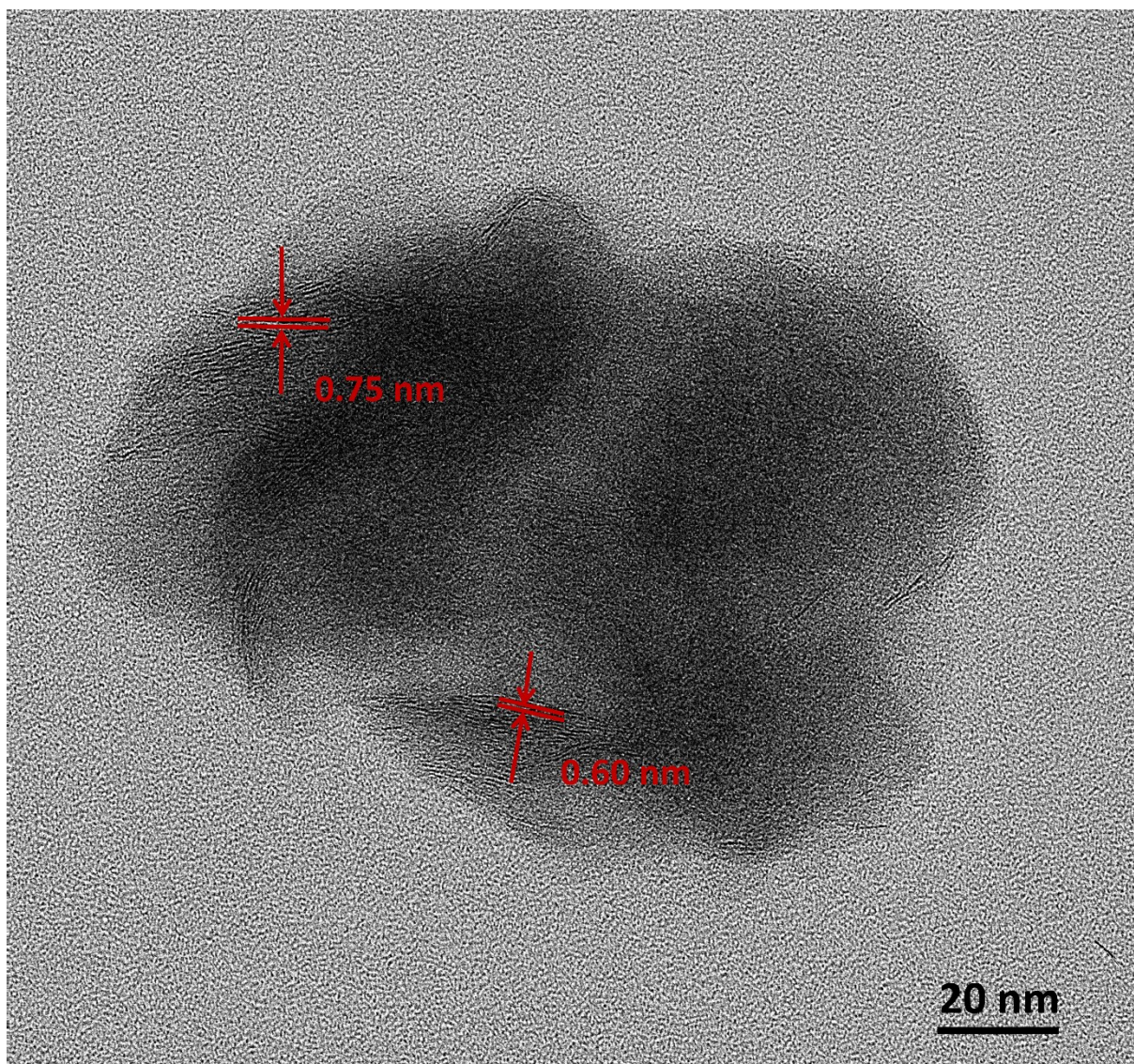


**Fig. S20.** HRTEM image of pristine MoS<sub>2</sub>. The interlayer space is in the range of 0.60~0.75 nm, which is similar to the lectures.<sup>6</sup>



**Fig. S21.** Magnified HRTEM image of Fig. 4B. The curved layers and irregular edges can be clearly observed. Considering the weak MoS<sub>2</sub> signals in XRD and Raman spectra, the abundance of segmented regions with distinct lattice fringe of ~0.27 nm on the MoS<sub>2</sub> planes are probably assigned to the crystallized TM sulfide.<sup>8</sup> It has been reported that the charge transfer may be heavily restricted because the electron and hole mobility between the sheets is about 2200 times slower than along the basal plane.<sup>9</sup> The existence of TM sulfide with metal-like conductivity may greatly increase the electronic conductivity and promote the HER process.<sup>10</sup>

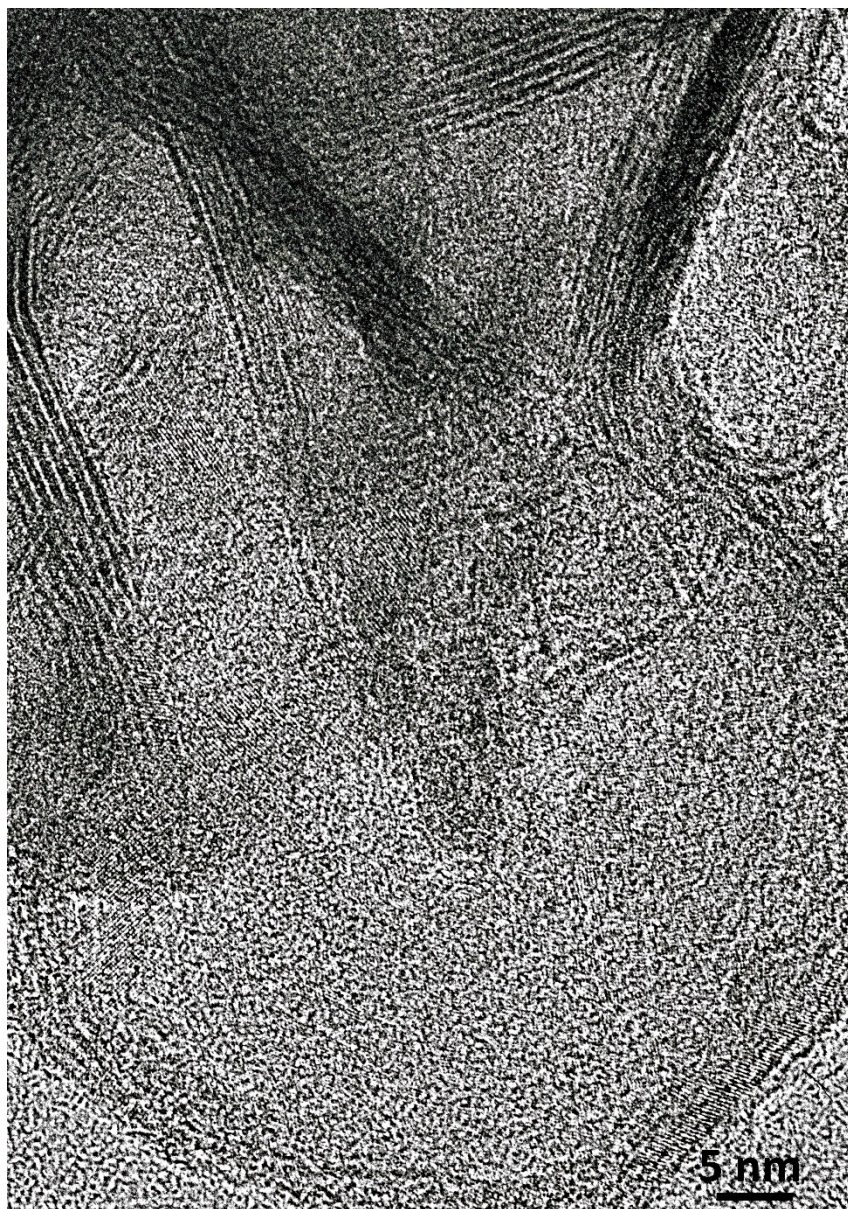


**Fig. S22.** Magnified HRTEM image of Fig. 4D. A lot of segments with distinct lattice fringe of  $\sim 0.27$  nm on the MoS<sub>2</sub> planes should be assigned to the crystallized transition metal sulfide. The curved layers and irregular edges can be clearly observed.

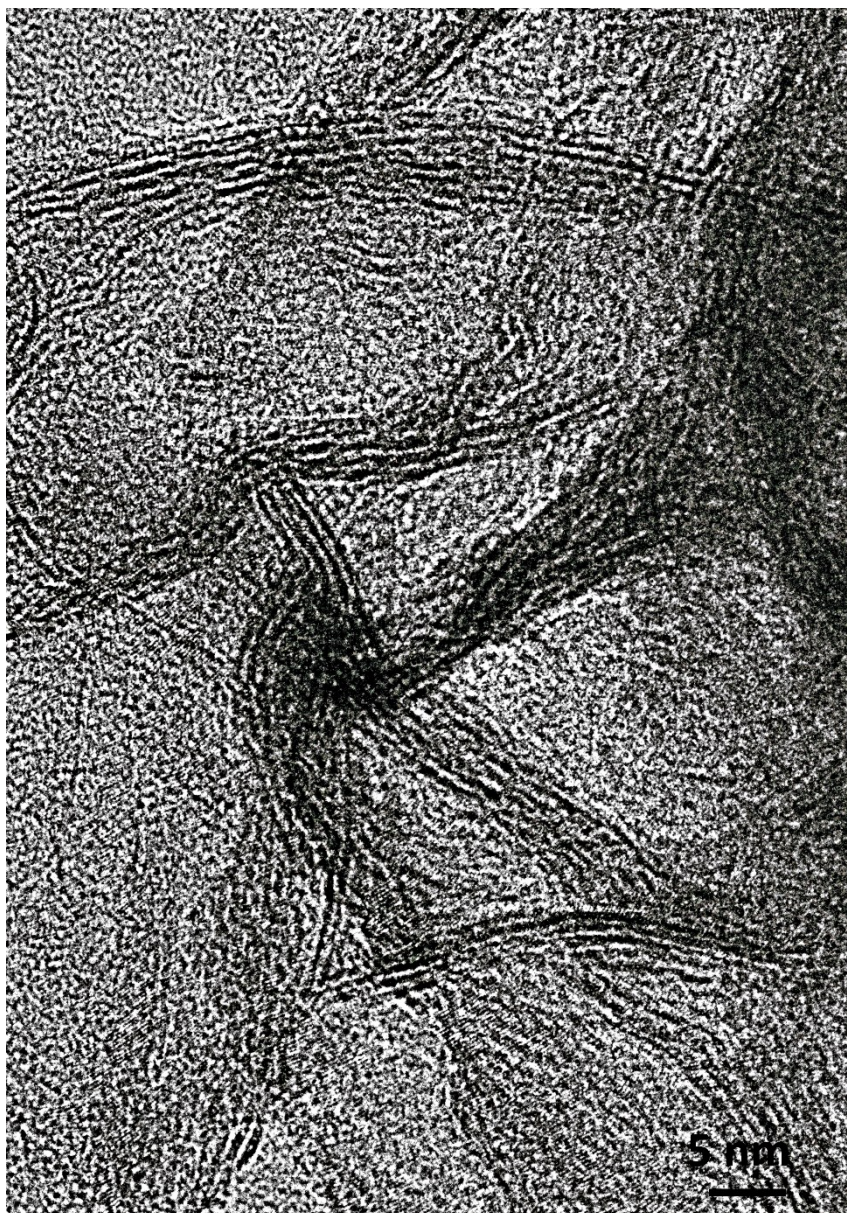


**Fig. S23.** Magnified HRTEM image of Fig. S19. A lot of segments with distinct lattice fringe of  $\sim 0.27$  nm on the MoS<sub>2</sub> planes should be assigned to the crystallized transition metal sulfide. The curved layers and irregular edges can be clearly observed.

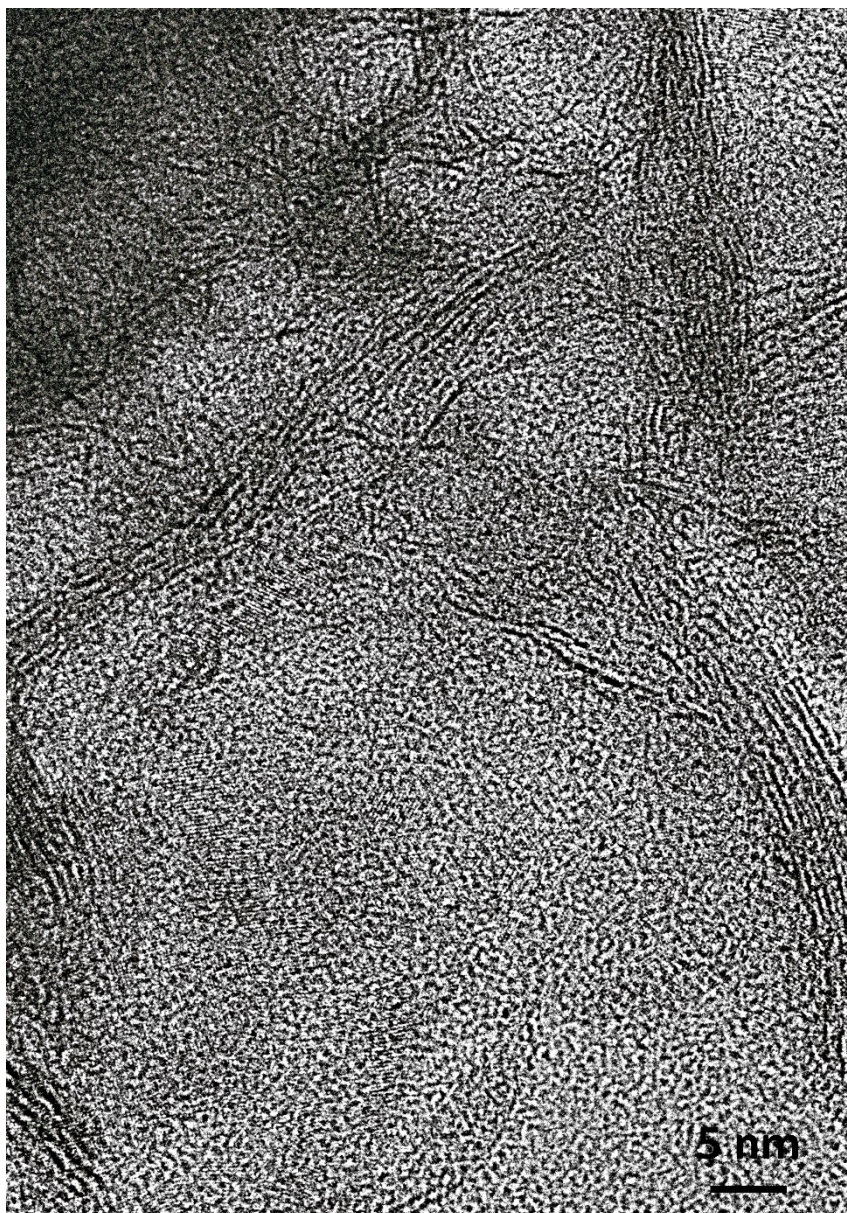


**Fig. S24.** Magnified HRTEM image of Fig. S19. A lot of segments with distinct lattice fringe of  $\sim 0.27$  nm on the MoS<sub>2</sub> planes should be assigned to the crystallized transition metal sulfide. The curved layers and irregular edges can be clearly observed.

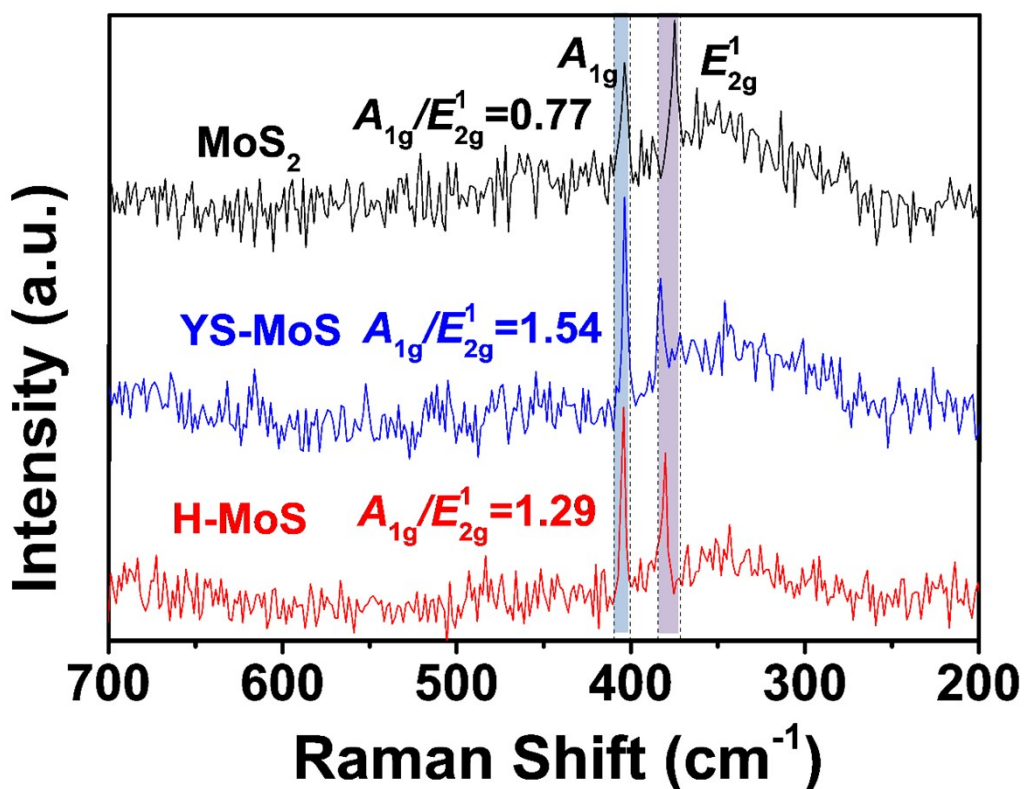


**Fig. S25.** Raman spectra of MoS<sub>2</sub>, H-MoS and YS-MoS. Two Raman peaks at 375 cm<sup>-1</sup> and 401.5 cm<sup>-1</sup> in pristine MoS<sub>2</sub> are corresponding to the in-plane (E<sub>12g</sub>) and out-of-plane (A<sub>g</sub>) Mo-S modes of the layered structure, respectively.<sup>4b,11</sup> The two peaks can also be observed in the very neighboring regions in H-MoS and YS-MoS. Compared to MoS<sub>2</sub>, the relative intensity of A<sub>1g</sub>/E<sub>12g</sub><sup>1</sup> in H-MoS and YS-MoS is higher, suggesting the more edge-terminated structure and the more defect sites in plane.<sup>4a,4b,11a,12</sup> However, the signals of the two peaks are very weak, indicating that the quantity of crystalline MoS<sub>2</sub> is not predominant,<sup>12-13</sup> as also suggested by the weak XRD peaks.

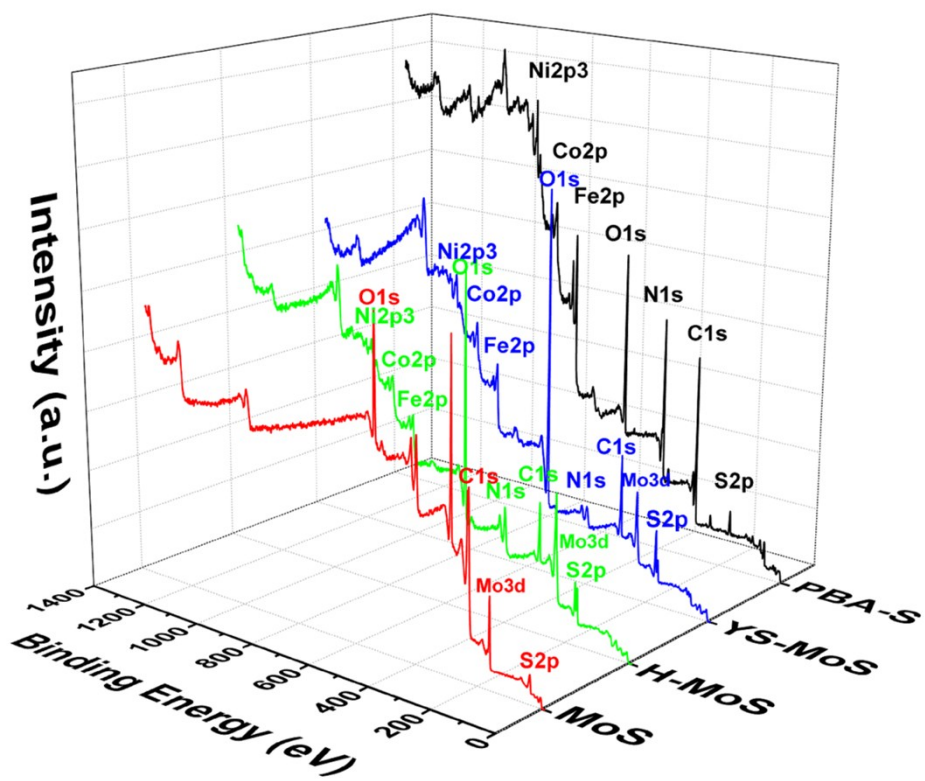
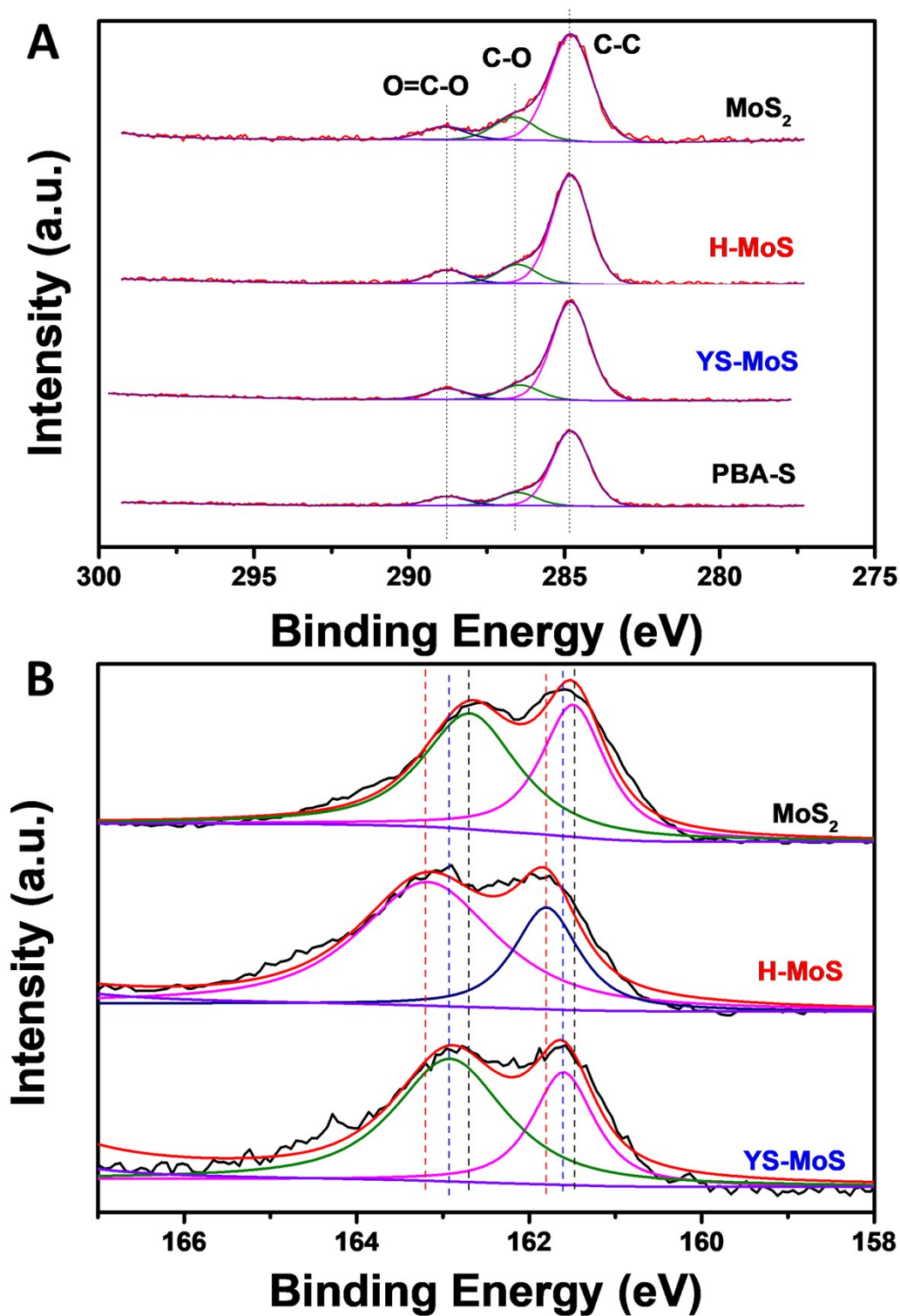


Fig. S26. XPS Survey spectra of YS-MoS, H-MoS, bare MoS<sub>2</sub> and PBA-S.

**Table S1.** The atomic ratio of YS-MoS, H-MoS, bare MoS<sub>2</sub> and PBA-S obtained from XPS spectra.

| Elem.            | Fe    | Co    | Ni    | Mo    | S     |
|------------------|-------|-------|-------|-------|-------|
| PBA-S            | 38.37 | 21.27 | 16.69 | -     | 23.67 |
| H-MoS            | 15.70 | 9.80  | 7.25  | 14.04 | 53.20 |
| YS-MoS           | 15.32 | 8.53  | 6.47  | 15.58 | 54.10 |
| MoS <sub>2</sub> | -     | -     | -     | 26.46 | 73.54 |

Clearly, the M (M=Fe, Co, Ni) content in the surface region is very high, confirming that Fe, Co, Ni are well doped in the MoS<sub>2</sub> nano-sheets. Fe, Co and Ni doping can increase the surface area, promote the growth and enhance the intrinsic catalysis of the highly active MoS<sub>3</sub>.<sup>14</sup> The atomic ratio of Mo and S in the pristine MoS<sub>2</sub> is close to 1:3, i.e. the dominance should be MoS<sub>3</sub> (MoS<sub>2</sub>S, S<sub>2</sub><sup>2-</sup> and S<sup>2-</sup>).<sup>13,15</sup> The shoulder peaks at ~161 eV and ~162 eV with a broad full width at the half- height of ~2.2 eV corresponding to the S 2p (Fig. S24B), indicating the existence of multiple oxidation states of terminal S<sup>2-</sup> and S<sub>2</sub><sup>2-</sup>,<sup>16</sup> which allows superior HER activity<sup>12-13,15,17</sup> and engenders more active sites number.<sup>18</sup> The relative contents of S element in H-MoS and YS-MoS are 53.20 % and 54.10 %, far lower than that in pristine MoS<sub>2</sub> (73.54 %). The low S content is probably due to the formation of TM-sulfide (M= Fe, Co, Ni) with low S atomic ratio.



**Fig. S27.** Define XPS spectra of (A) C for YS-MoS, H-MoS, bare MoS<sub>2</sub> and PBA-S, and (B) S for YS-MoS, H-MoS<sub>2</sub> and PBA-S. All the peaks have been calibrated by setting the main C peak at 284.8 eV.

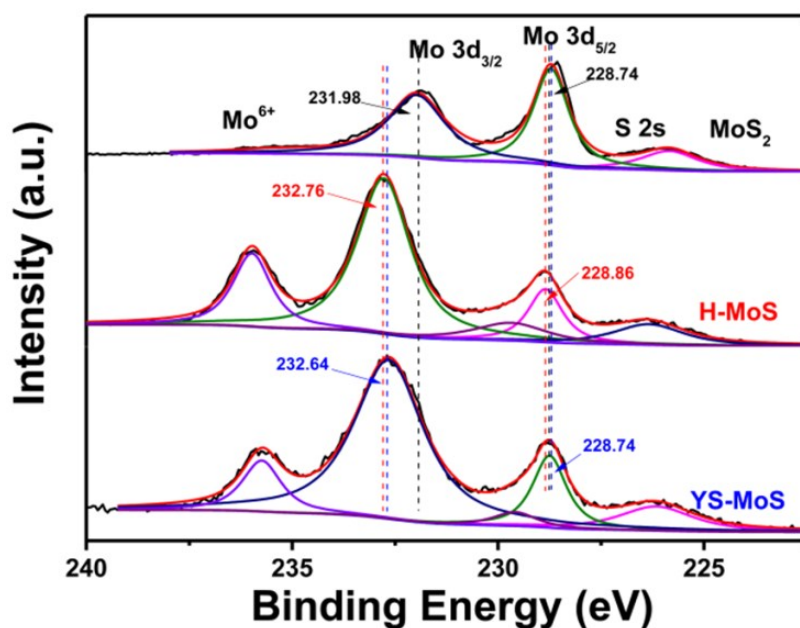


**Fig. S28.** XPS spectra of Mo for MoS<sub>2</sub>, H-MoS and YS-MoS. The peaks at ~226 eV correspond to the S 2s.<sup>12,19</sup> Compared with pristine MoS<sub>2</sub>, the Mo (VI) peaks in H-MoS and YS-MoS are much higher, and the peaks for Mo 3d<sub>3/2</sub> also show an increase at higher binding energy. The weak peaks of 229.58 eV for YS-MoS and 229.70 eV for H-MoS could be attributed to Mo (V).<sup>12</sup> The peaks at ~232 eV can be assigned to the MoS<sub>2</sub>(IV)<sup>20</sup> and the peak at ~236 eV should be Mo(VI).<sup>12-13,20a</sup> It is interesting that the contents of Mo(VI) in H-MoS and YS-MoS are much higher than that in the pristine MoS<sub>2</sub>, and the relative intensity of Mo 3d<sub>3/2</sub> to Mo 3d<sub>5/2</sub> increases significantly in H-MoS and YS-MoS, which has been observed in MoS<sub>2</sub>/Co<sub>9</sub>S<sub>8</sub> system.<sup>21</sup>

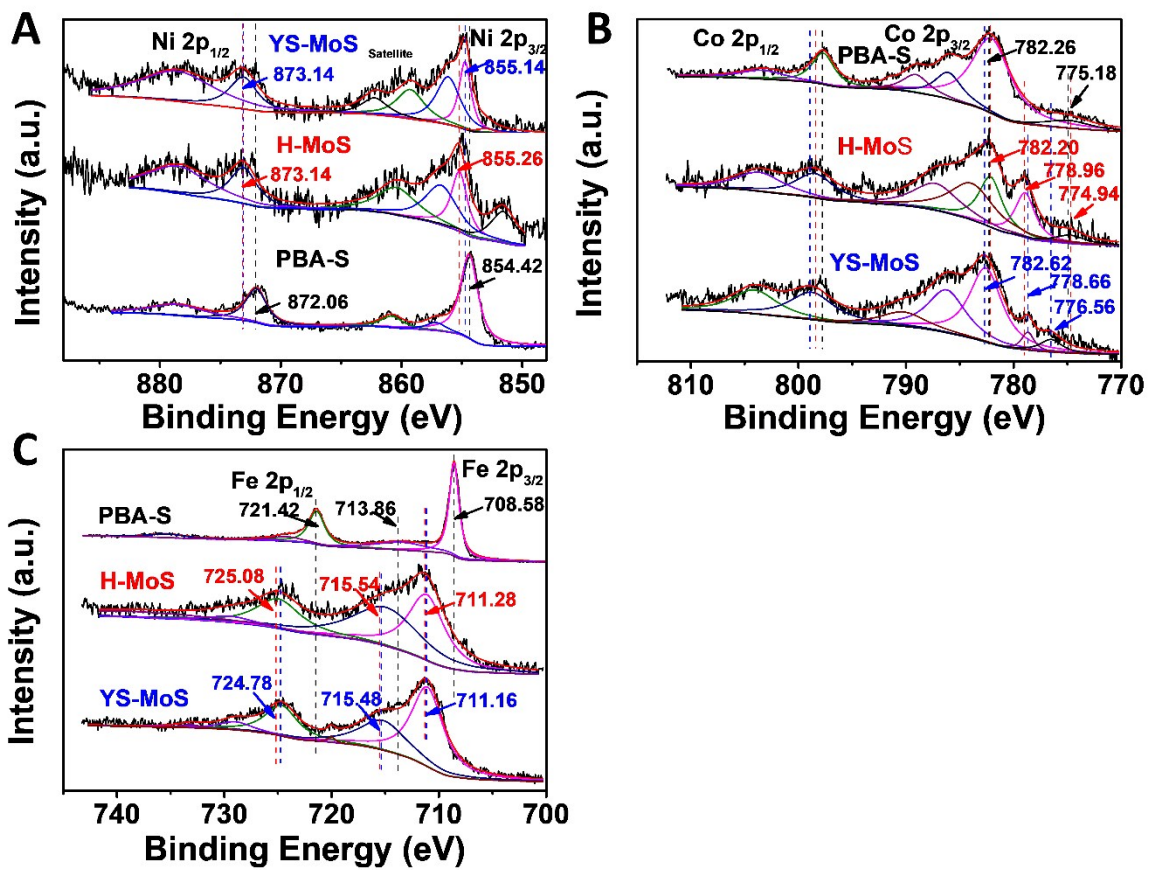
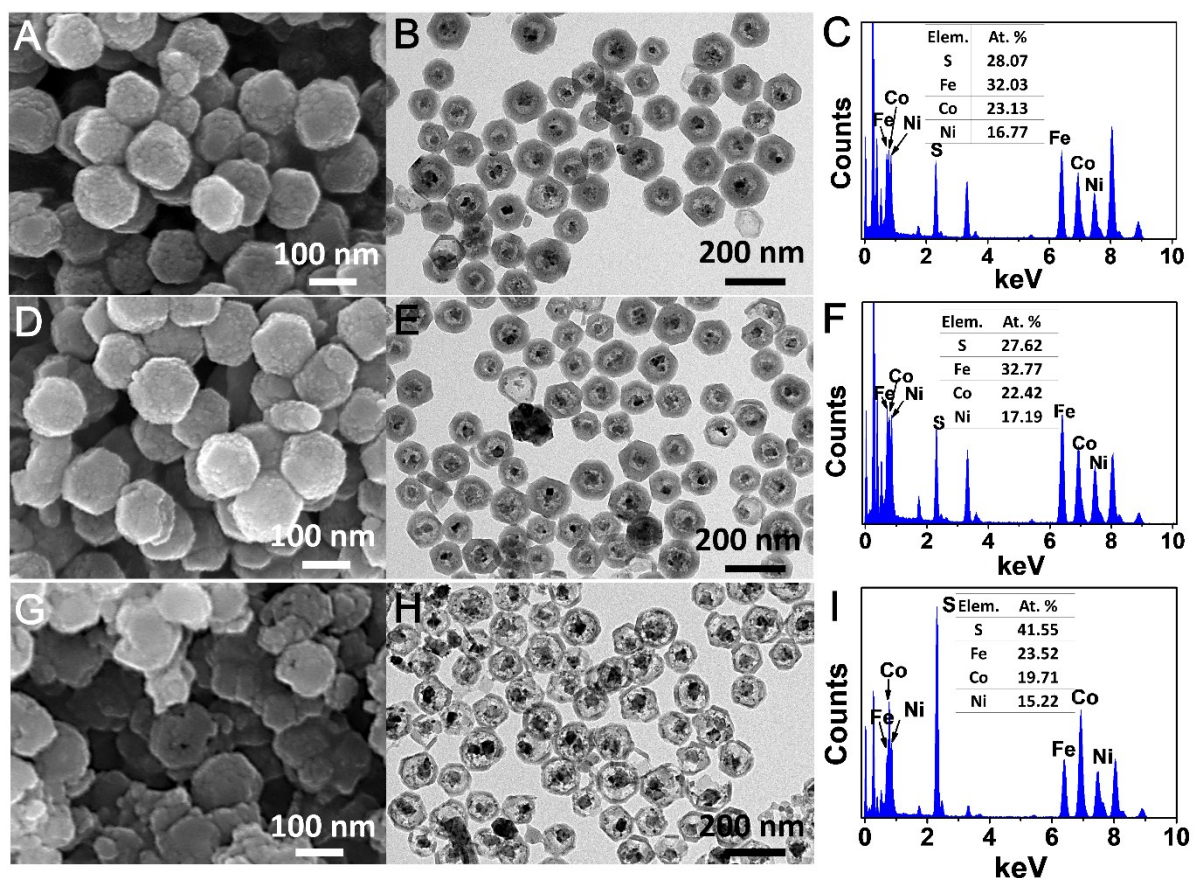
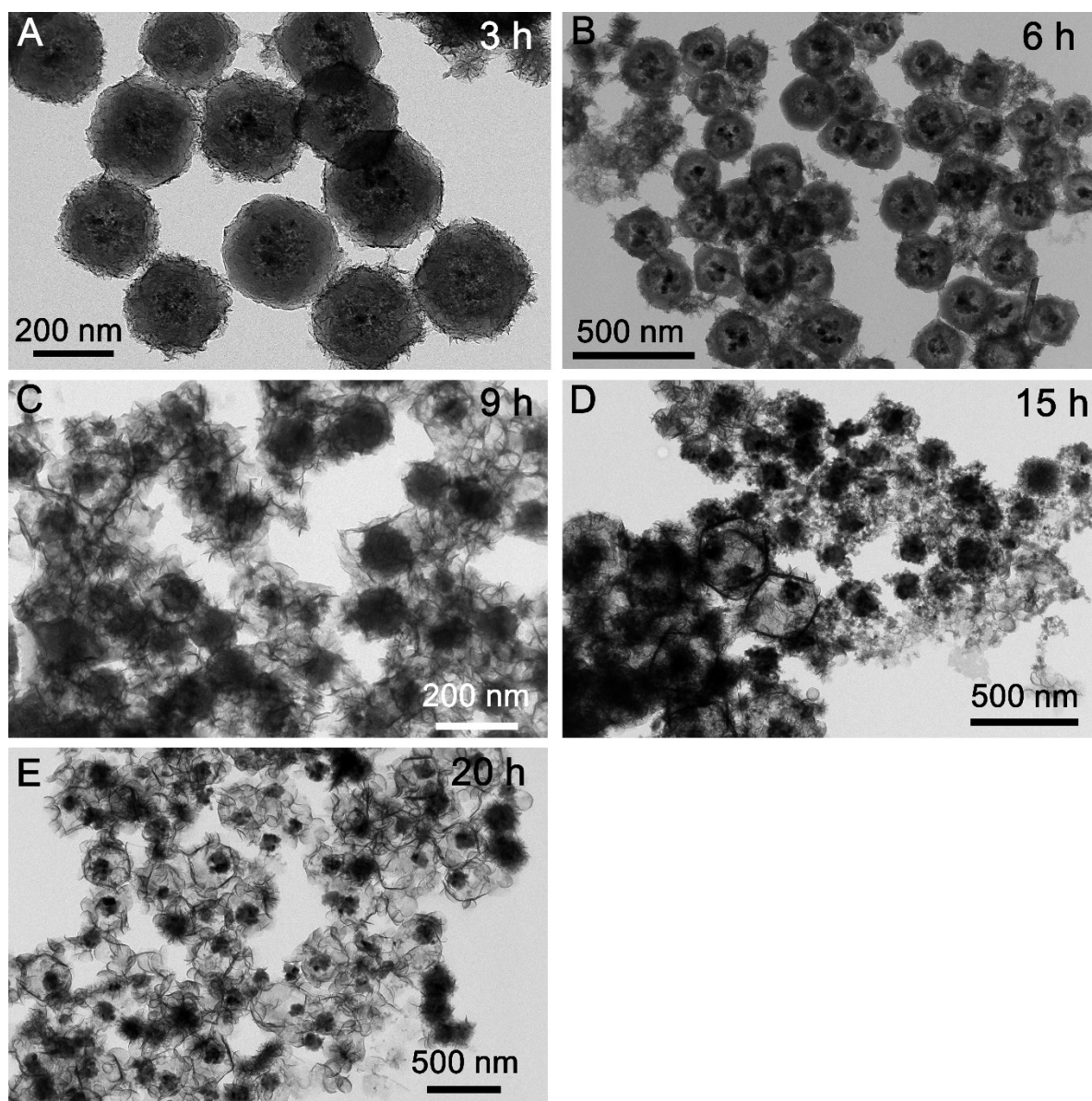


Fig. S29. Define XPS spectra of (A) Ni, (B) Co and (C) Fe for YS-MoS, H-MoS<sub>2</sub> and PBA-S.



**Fig. S30.** SEM, TEM images, EDS spectra and the corresponding compositions of the products obtained by reacting CoNi-Fe PBA (28 mg) with S powder (3 mg) in DMF at various temperature. (A) 170 °C, (B) 190 °C and (C) 210 °C. The PBA surface reacted with oxygen/S and formed a firm oxide/sulfide shell. In DMF, the outward diffusion of metal ions was restrained, and S entered the polyhedra through the porous shell and formed a TMS yolk. Simultaneously, the TMS yolk shrunk and separated with the firm shell due to the density discrepancy between the sulfides and PBA precursor, and a yolk-shell structure eventually formed. The yolk-shell products at 190 °C have regular polyhedral shape, suitable shell and yolk, which were then applied for the generation of YS-MoS.



**Fig. S31.** YS-MoS Products at different reaction time of (A) 3 h, (B) 6 h, (C) 9 h, (E) 15 h, (F) 20 h. Small nanosheets can be observed (3h) and grew larger (6h), at the same time, the shells of PBA-S became thinner. At 9 h, the shells disappeared and the nanosheets grew larger around the yolks and interlaced together. The nanosheets assembled as hollow boxes around the yolks (15h, 20 h). The yolks preserved through the process.

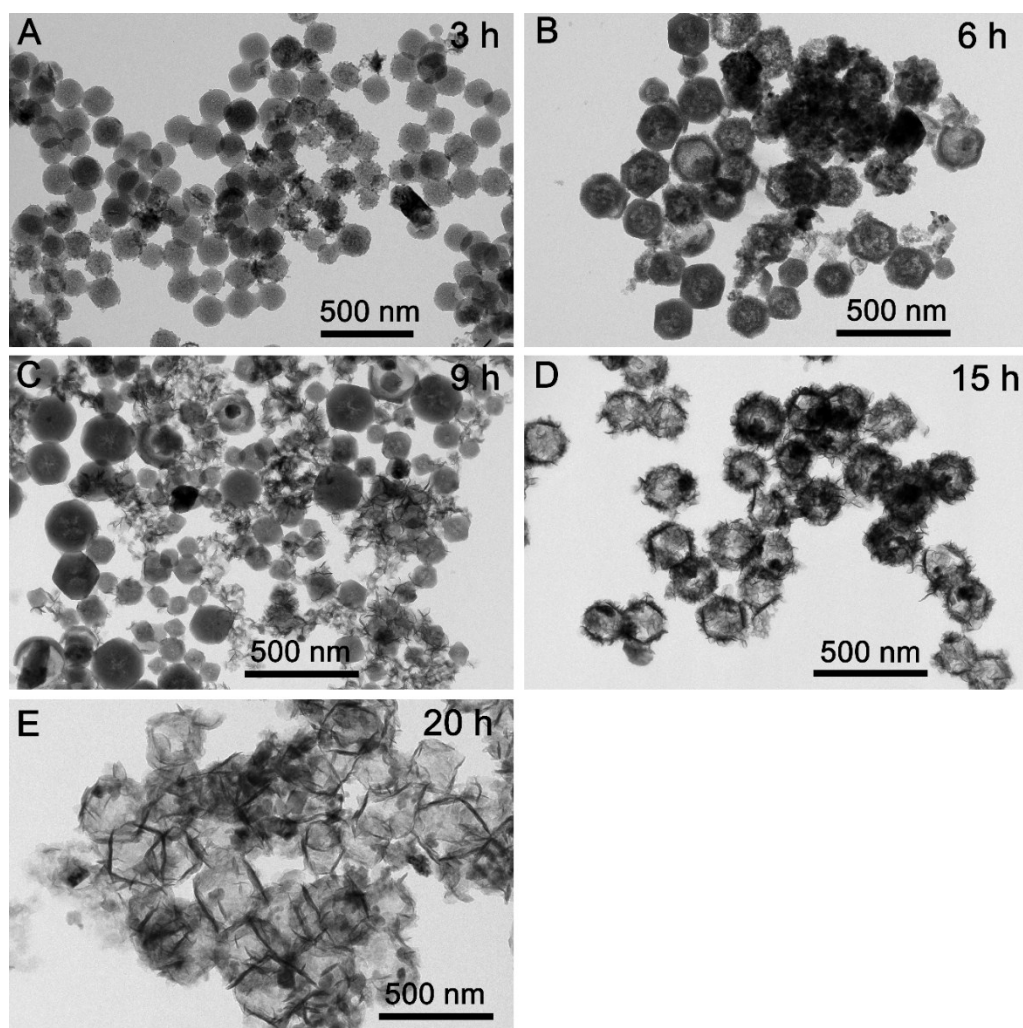


**Fig. S32.** H-MoS Products at different reaction time of (A) 3 h, (B) 6 h, (C) 9 h, (E) 15 h, (F) 20 h. The polyhedral PBA became rough (3h) and hollow (6h), at the same time, some small nanosheets can be observed. The PBA etching and MoS<sub>2</sub> growth concurrently happened. The etching speed of the center was faster than the shell. As the cavity in PBA became larger, the shell became thinner. At the same time, the MoS<sub>2</sub> NS grew larger. The PBA became more hollow and the nanosheets grew larger (15 h). At 20 h, PBA disappeared completely and the products are hollow box assembled with nanosheets. During this process, amino groups released from (NH<sub>4</sub>)<sub>2</sub>MoS<sub>4</sub> adsorbed on PBA surface as nucleation sites for catching Mo species. MoS<sub>2</sub> NS produced from solvothermal reaction of (NH<sub>4</sub>)<sub>2</sub>MoS<sub>4</sub> and grew at these nucleation sites. Meanwhile, the released TM (Fe, Co, Ni) ions met with MoS<sub>4</sub><sup>2-</sup> on the as-generated MoS<sub>2</sub> NS and formed crystal TMS, new phases of MMoS (M=Ni, Co, Fe) in-situ formed as well. Eventually, hollow box of MoS<sub>2</sub> NS with TM (Ni, Co, Fe) doping (H-MoS) were obtained.

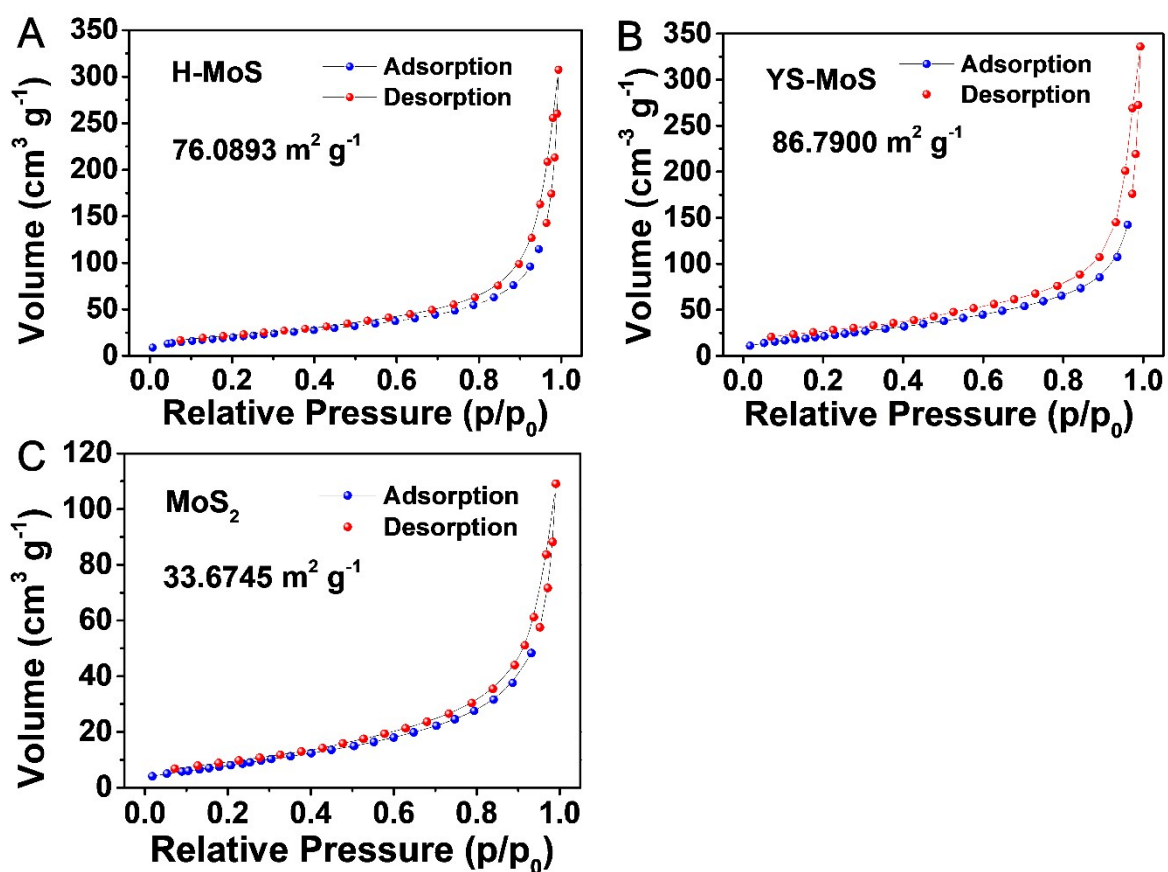


**Fig. S33.** Nitrogen adsorption-desorption isotherms of YS-MoS, H-MoS and bare MoS. Although core-shell or yolk-shell TM-MoS<sub>3</sub> has been synthesized via a one-pot template-engaged precipitation process. Our product is much superior to the previously reported hollow box, which assembled by MoS<sub>2</sub> particles with a very low BET of  $24 \text{ m}^2 \text{g}^{-1}$ .<sup>22</sup>

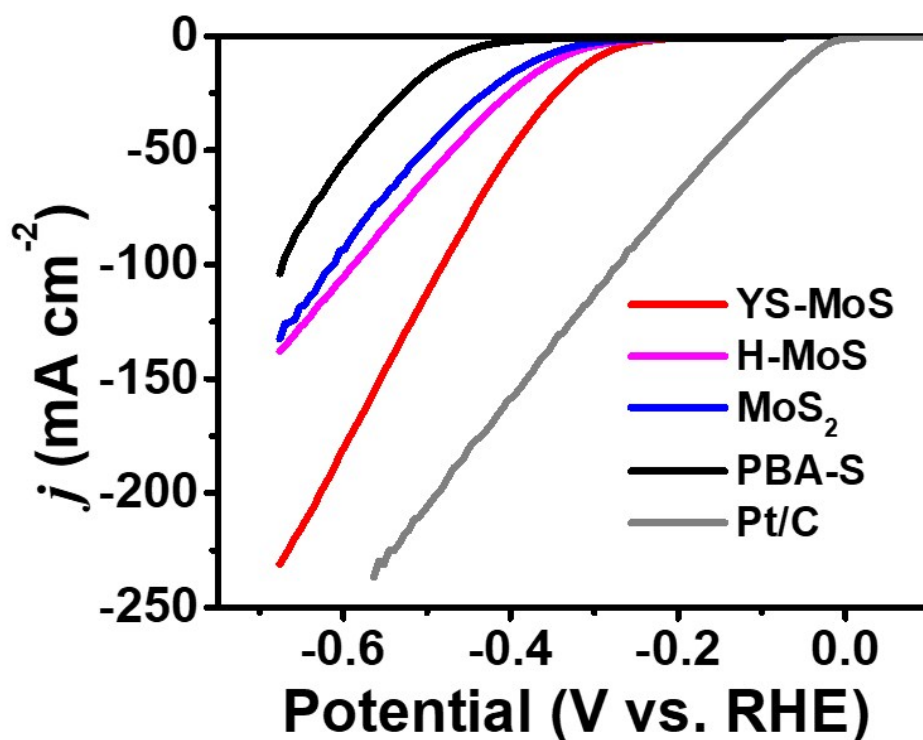


**Fig. S34.** HER polarization curves of YS-MoS, H-MoS, MoS<sub>2</sub> and PBA-S without IR-correction. To avoid shedding and achieve maximum utilizations, all the catalysts were loaded on carbon black and anchored onto the RDE with Nafion.<sup>1,23</sup> As expected, the PBA-S displays the lowest activity with an onset potential of -305 mV. YS-MoS shows the smallest onset potential of -186 mV, which is even less than those of pristine MoS<sub>2</sub> (-251 mV) and H-MoS (-233 mV). In addition, the cathode current of YS-MoS increased much sharply at more negative potential than the other catalysts.

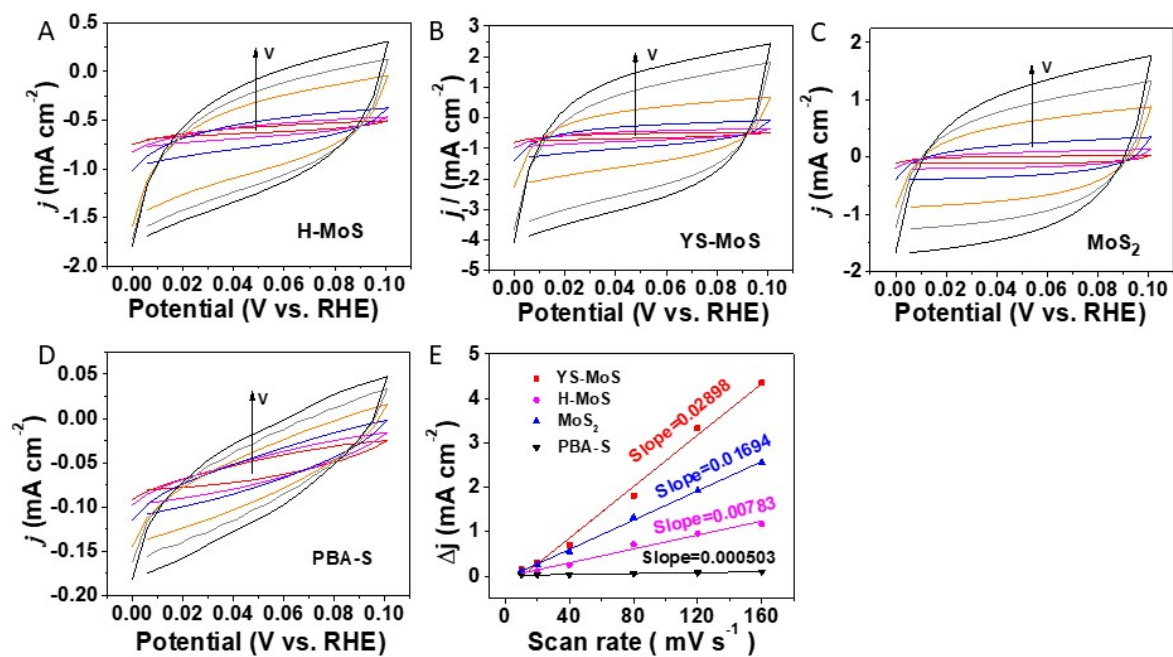


**Fig. S35.** Cyclic voltammograms curves of various samples at the scan rate ranging from 10 to 160  $\text{mV s}^{-1}$  with an interval point of 20  $\text{mV s}^{-1}$  in 1.0 M KOH upon HER catalysis for the determination of the double layer capacitance: (A) H-MoS, (B) YS-MoS, (C) MoS<sub>2</sub> and (D) PBA-S. (E) Plots of current densities versus scan rates. YS-MoS obtains the highest double layer capacitance.

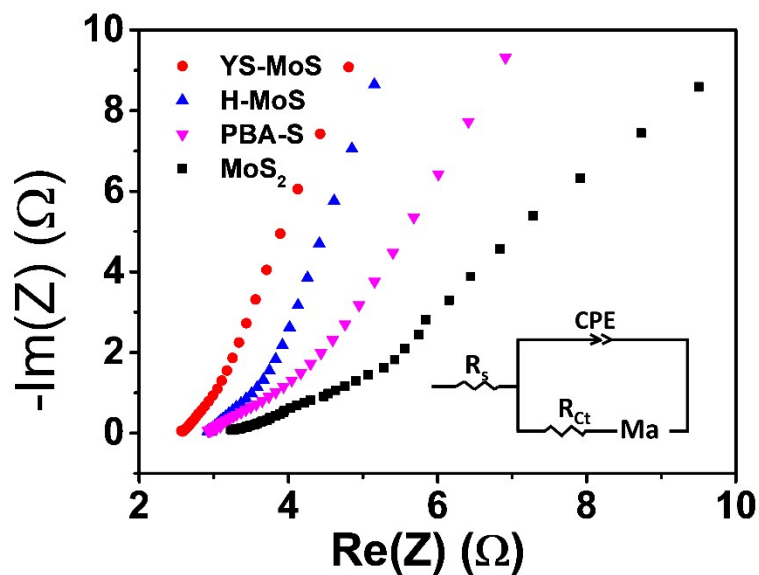


**Fig. S36.** Electrochemical impedance spectroscopy (EIS) Nyquist plots for YS-MoS, H-MoS, PBA-S and MoS<sub>2</sub> at open circuit voltage. All the electrodes can be modelled by using a modified Randles circuit inclusive of a series resistance ( $R_s$ ), constant phase element (CPE), charge transfer resistance ( $R_{ct}$ ) and a modified mass transport impedance element (Ma). The semicircular arc assigned to CPE and  $R_{ct}$  impedance elements seen for MoS<sub>2</sub> significantly decreased and almost disappeared in YS-MoS, mainly due to the faster charge transfer and the larger surface area.<sup>24</sup>

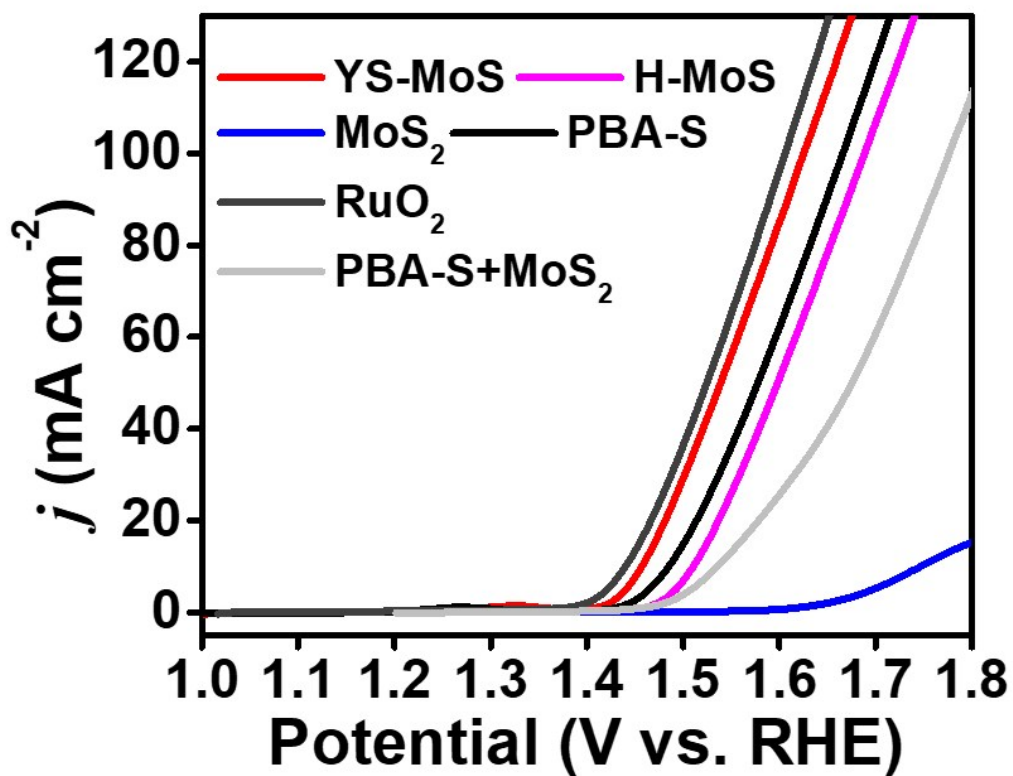


**Fig. S37.** OER polarization curves of YS-MoS, H-MoS, MoS<sub>2</sub>, PBA-S, RuO<sub>2</sub> and MoS<sub>2</sub>+PBA-S without IR-correction. The sample of MoS<sub>2</sub>+PBA-S is the mixture of MoS<sub>2</sub> and PBA-S. The performance of MoS<sub>2</sub>+PBA-S is inferior than PBA-S and H-MoS because that i) no synergetic effect between MoS<sub>2</sub> with PBA-S, ii) no transition metal doping in MoS<sub>2</sub>+PBA-S sample.

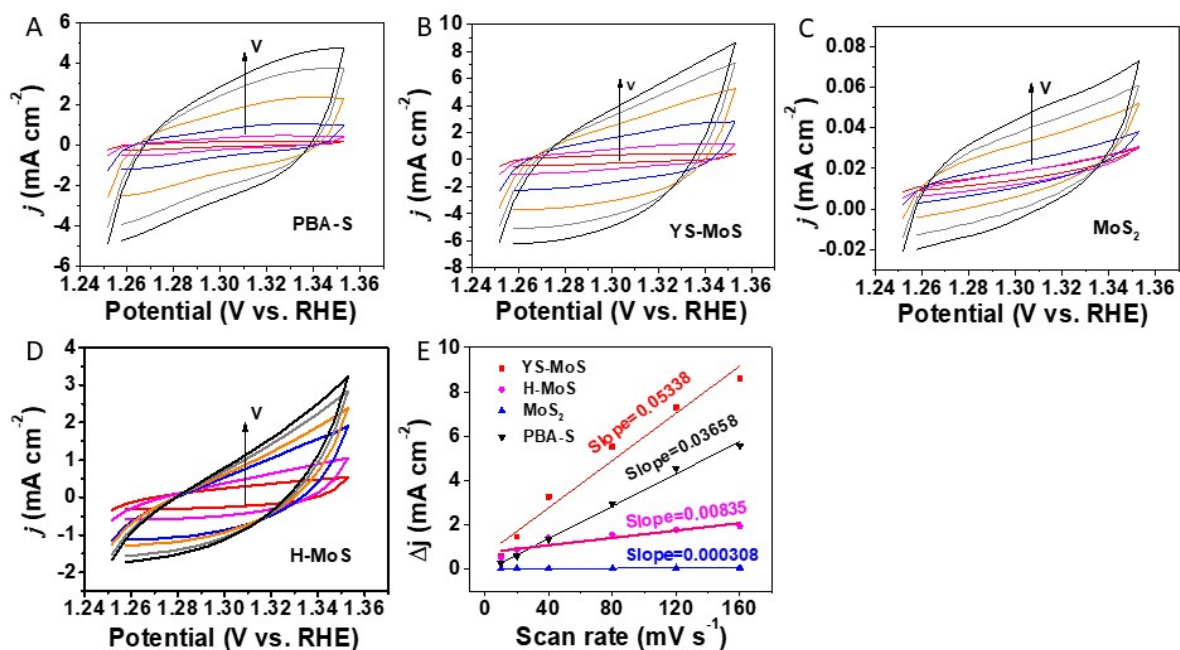


**Fig. S38.** Cyclic voltammograms curves of various samples at the scan rate ranging from 10 to 160  $\text{mV s}^{-1}$  with an interval point of 20  $\text{mV s}^{-1}$  in 1.0 M KOH upon OER catalysis for the determination of the double layer capacitance: (A) PBA-S, (B) YS-MoS, (C) MoS<sub>2</sub> and (D) H-MoS. (E) Plots of current densities versus scan rates. YS-MoS obtains the highest double layer capacitance.

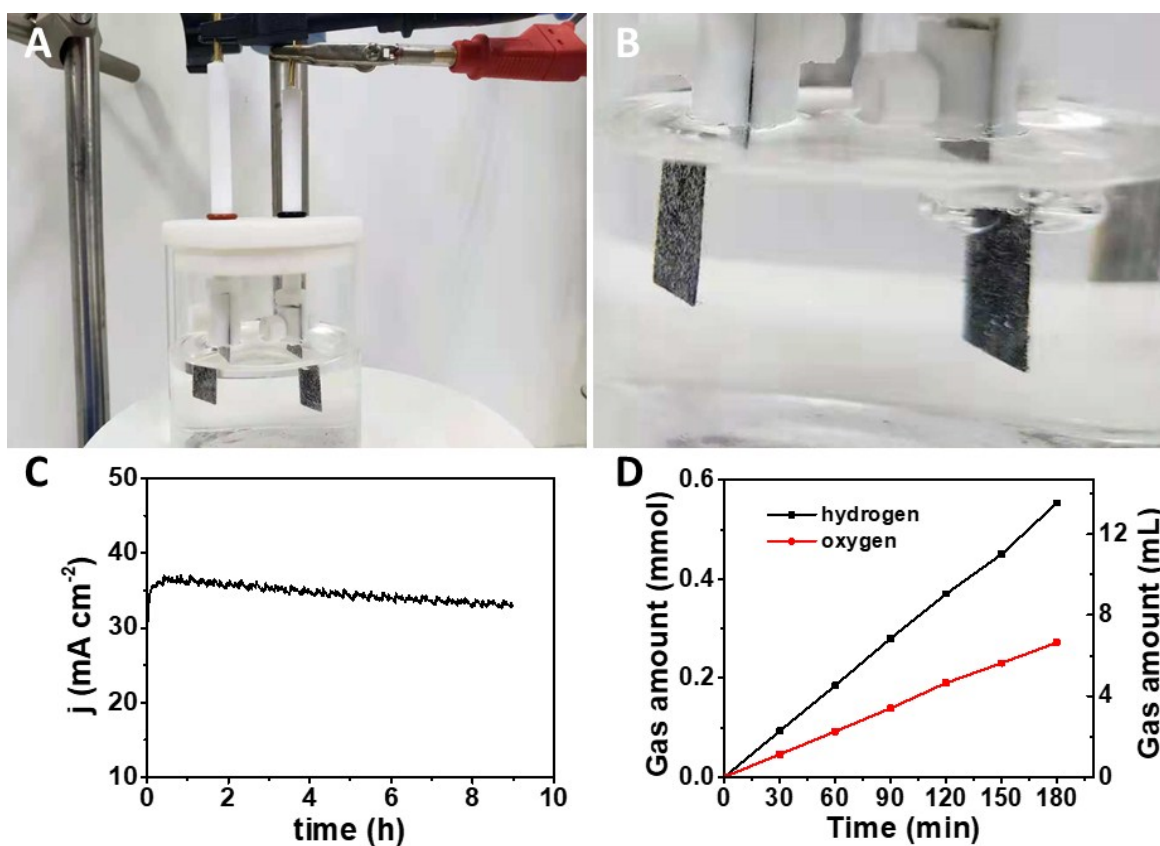


**Fig. S39.** (A) Demonstration of the two-electrode system for water splitting, (B) The gas produced on the electrodes, (C) The I-t curve of the two electrode system at DC 2.0 V. (D) The collected hydrogen and oxygen amount at a current density of 10 mA at 298 K, the two electrodes were separated completely. The amount of hydrogen and oxygen shows a molar ratio close to 2:1. The faradic efficiencies of HER and OER are 99 % and 95%, respectively.

**Table S2.** HER and OER over-potential at 10 mA cm<sup>-2</sup> in 1.0 M KOH.

| Catalysts  | Over-potential (mV vs. RHE)<br>at 10 mA cm <sup>-2</sup> |     | Ref.      |
|--|--|-----|-----------|
|  | HER  | OER |           |
| YS-MoS   | 285  | 178 | This work |
| H-MoS  | 329  | 228 | This work |
| MoS <sub>2</sub> nano-sheets                               | 354  | 512 | This work |
| PBA-S  | 465  | 196 | This work |
| Co <sub>9</sub> S <sub>8</sub> @MoS <sub>2</sub>           | 143  | 342 | 21        |
| Co <sub>9</sub> S <sub>8</sub>                             | 461  | 384 | 21        |
| MoS <sub>2</sub>   | 202  | 486 | 21        |
| Co <sub>9</sub> S <sub>8</sub> &MoS <sub>2</sub>           | 389  | -   | 21        |
| CoNC@MoS <sub>2</sub> /CNF                                 | 143  | 350 | 25        |
| MoS <sub>2</sub> -Ni <sub>3</sub> S <sub>2</sub> /CNF      | 98   | 249 | 26        |
| MoS <sub>2</sub> /Ni <sub>3</sub> S <sub>2</sub> particles | 110  | 218 | 19        |
| CoS-Co(OH) <sub>2</sub> @MoS <sub>2+x</sub> /NF            | 143  | 380 | 27        |
| NiS-Ni(OH) <sub>2</sub> @MoS <sub>2+x</sub> /NF            | 226  | 417 | 27        |
| Mo-N/C@MoS <sub>2</sub>                                    | 117  | -   | 28        |
| Co <sub>9</sub> O <sub>8</sub> /CNFs                       | -  | 512 | 29        |
| Co <sub>9</sub> S <sub>8</sub> @MoS <sub>2</sub> /CNFs     | -  | 430 | 29        |
| Ni/graphene-MoS <sub>2</sub>                               | -  | 214 | 30        |
| Ni <sub>2</sub> P/MoO <sub>2</sub> @MoS <sub>2</sub>       | 159  | 280 | 31        |
| Ultrafine MoS <sub>2</sub> on Co foam                      | -  | 271 | 20a       |
| Co covalent doping in MoS <sub>2</sub>                     | 48   | 260 | 32        |
| Amorphous Ni-Co hybridized with 1T- MoS <sub>2</sub>       | 70   | 235 | 33        |

## References

- 1 H. Li, S. Chen, X. Jia, B. Xu, H. Lin, H. Yang, L. Song and X. Wang, *Nat. Commun.*, 2017, **8**, 15377.
- 2 Tong Liu, Anran Li, Chengbo Wang, Wei Zhou, Shijie Liu and L. Guo, *Adv. Mater.*, 2018, 1803590.
- 3 Q. Liu and J. Zhang, *CrystEngComm*, 2013, **15**, 5087-5092.
- 4 (a) X.-Y. Yu, Y. Feng, Y. Jeon, B. Guan, X. W. Lou and U. Paik, *Adv. Mater.*, 2016, **28**, 9006-9011; (b) M.-R. Gao, M. K. Y. Chan and Y. Sun, *Nat. Commun.*, 2015, **6**, 7493; (c) Q. Liu, X. Li, Q. He, A. Khalil, D. Liu, T. Xiang, X. Wu and L. Song, *Small*, 2015, **11**, 5556-5564.
- 5 Y. Sun, S. Gao, F. Lei and Y. Xie, *Chem. Soc. Rev.*, 2015, **44**, 623-636.
- 6 (a) H. Zhang, Y. Li, T. Xu, J. Wang, Z. Huo, P. Wan and X. Sun, *J. Mater. Chem. A*, 2015, **3**, 15020-15023; (b) X. Zuo, K. Chang, J. Zhao, Z. Xie, H. Tang, B. Li and Z. Chang, *J. Mater. Chem. A*, 2016, **4**, 51-58.
- 7 (a) J. Xie, J. Zhang, S. Li, F. Grote, X. Zhang, H. Zhang, R. Wang, Y. Lei, B. Pan and Y. Xie, *J. Am. Chem. Soc.*, 2013, **135**, 17881-17888; (b) J. Deng, H. Li, S. Wang, D. Ding, M. Chen, C. Liu, Z. Tian, K. S. Novoselov, C. Ma, D. Deng and X. Bao, *Nat. Commun.*, 2017, **8**, 14430.
- 8 Y. Guo, L. Gan, C. Shang, E. Wang and J. Wang, *Adv. Funct. Mater.*, 2017, **27**, 1602699.
- 9 Y. Yu, S.-Y. Huang, Y. Li, S. N. Steinmann, W. Yang and L. Cao, *Nano Lett.*, 2014, **14**, 553-558.
- 10 (a) M. S. Faber, R. Dziedzic, M. A. Lukowski, N. S. Kaiser, Q. Ding and S. Jin, *J. Am. Chem. Soc.*, 2014, **136**, 10053-10061; (b) H. Zhang, Y. Li, G. Zhang, T. Xu, P. Wan and X. Sun, *J. Mater. Chem. A*, 2015, **3**, 6306-6310.
- 11 (a) D. Kong, H. Wang, J. J. Cha, M. Pasta, K. J. Koski, J. Yao and Y. Cui, *Nano Lett.*, 2013, **13**, 1341-1347; (b) H. Wang, Z. Lu, D. Kong, J. Sun, T. M. Hymel and Y. Cui, *ACS Nano*, 2014, **8**, 4940-4947; (c) J. Kibsgaard, Z. Chen, B. N. Reinecke and T. F. Jaramillo, *Nat. Mater.*, 2012, **11**, 963-969; (d) H. Li, Q. Zhang, C. C. R. Yap, B. K. Tay, T. H. T. Edwin, A. Olivier and D. Baillargeat, *Adv. Funct. Mater.*, 2012, **22**, 1385-1390.
- 12 X. Dai, K. Du, Z. Li, M. Liu, Y. Ma, H. Sun, X. Zhang and Y. Yang, *ACS Appl. Mater. Interfaces*, 2015, **7**, 27242-27253.
- 13 J. D. Benck, Z. Chen, L. Y. Kuritzky, A. J. Forman and T. F. Jaramillo, *ACS Catal.*, 2012, **2**, 1916-1923.
- 14 D. Merki, H. Vrubel, L. Rovelli, S. Fierro and X. Hu, *Chem. Sci.*, 2012, **3**, 2515-2525.
- 15 C. G. Morales-Guio and X. Hu, *Acc. Chem. Res.*, 2014, **47**, 2671-2681.
- 16 (a) J. Kibsgaard, T. F. Jaramillo and F. Besenbacher, *Nat. Chem.*, 2014, **6**, 248-253; (b) C.-H. Lee, J.-M. Yun, S. Lee, S. M. Jo, K. Eom, D. C. Lee, H.-I. Joh and T. F. Fuller, *Sci. Rep.*, 2017, **7**, 41190.
- 17 (a) M. L. Tang, D. C. Grauer, B. Lassalle-Kaiser, V. K. Yachandra, L. Amirav, J. R. Long, J. Yano and A. P. Alivisatos, *Angew. Chem. Int. Ed.*, 2011, **50**, 10203-10207; (b) D. Merki, S. Fierro, H. Vrubel and X. Hu, *Chem. Sci.*, 2011, **2**, 1262-1267; (c) H. Vrubel, D. Merki and X. Hu, *Energy Environ. Sci.*, 2012, **5**, 6136-6144.
- 18 Y.-H. Chang, R. D. Nikam, C.-T. Lin, J.-K. Huang, C.-C. Tseng, C.-L. Hsu, C.-C. Cheng, C.-Y. Su, L.-J. Li and D. H. C. Chua, *ACS Appl. Mater. Interfaces*, 2014, **6**, 17679-17685.
- 19 J. Zhang, T. Wang, D. Pohl, B. Rellinghaus, R. Dong, S. Liu, X. Zhuang and X. Feng, *Angew. Chem. Int. Ed.*, 2016, **55**, 6702-6707.
- 20 (a) D. Xiong, Q. Zhang, W. Li, J. Li, X. Fu, M. F. Cerqueira, P. Alpuim and L. Liu, *Nanoscale*, 2017, **9**, 2711-2717; (b) S. McDonnell, A. Azcatl, R. Addou, C. Gong, C. Battaglia, S. Chuang, K. Cho, A. Javey and R. M. Wallace, *ACS Nano*, 2014, **8**, 6265-6272.
- 21 J. Bai, T. Meng, D. Guo, S. Wang, B. Mao and M. Cao, *ACS Appl. Mater. Interfaces*, 2018, **10**, 1678-1689.
- 22 L. Yu, B. Y. Xia, X. Wang and X. W. Lou, *Adv. Mater.*, 2016, **28**, 92-97.
- 23 (a) B. Hinnemann, P. G. Moses, J. Bonde, K. P. Jørgensen, J. H. Nielsen, S. Horch, I. Chorkendorff and J. K. Nørskov, *J. Am. Chem. Soc.*, 2005, **127**, 5308-5309; (b) T. F. Jaramillo, J. Bonde, J. Zhang, B.-L. Ooi, K. Andersson, J. Ulstrup and I. Chorkendorff, *The Journal of Physical Chemistry C*, 2008, **112**, 17492-17498.
- 24 Miguel Cabán-Acevedo, Michael L. Stone, J. R. Schmidt, Joseph G. Thomas, Qi Ding, Hung-Chih Chang, Meng-Lin Tsai, Jr-Hau He and S. Jin, *Nat. Mater.*, 2015, **14**, 1245-1253.
- 25 D. Ji, S. Peng, L. Fan, L. Li, X. Qin and S. Ramakrishna, *J. Mater. Chem. A*, 2017, **5**, 23898-23908.
- 26 Y. Yang, K. Zhang, H. Lin, X. Li, H. C. Chan, L. Yang and Q. Gao, *ACS Catal.*, 2017, **7**, 2357-2366.
- 27 T. Yoon and K. S. Kim, *Adv. Funct. Mater.*, 2016, **26**, 7386-7393.
- 28 I. S. Amiinu, Z. Pu, X. Liu, K. A. Owusu, H. G. R. Monestel, F. O. Boakye, H. Zhang and S. Mu, *Adv. Funct. Mater.*, 2017, **27**, 1702300.

- 29 H. Zhu, J. Zhang, R. Yanzhang, M. Du, Q. Wang, G. Gao, J. Wu, G. Wu, M. Zhang, B. Liu, J. Yao and X. Zhang, *Adv. Mater.*, 2015, **27**, 4752-4759.
- 30 B. J. Waghmode, S. N. Bhange, S. M. Unni, K. R. Patil and D. D. Malkhede, *Sustainable Energy & Fuels*, 2017, **1**, 1329-1338.
- 31 Y. Wang, T. Williams, T. Gengenbach, B. Kong, D. Zhao, H. Wang and C. Selomulya, *Nanoscale*, 2017, **9**, 17349-17356.
- 32 Q. Xiong, Y. Wang, P.-F. Liu, L.-R. Zheng, G. Wang, H.-G. Yang, P.-K. Wong, H. Zhang and H. Zhao, *Adv. Mater.*, 2018, **30**, 1801450.
- 33 H. Li, S. Chen, X. Jia, B. Xu, H. Lin, H. Yang, L. Song and X. Wang, *Nat. Commun.*, 2017, **8**, 15377.